



저작자표시-비영리-변경금지 2.0 대한민국

이용자는 아래의 조건을 따르는 경우에 한하여 자유롭게

- 이 저작물을 복제, 배포, 전송, 전시, 공연 및 방송할 수 있습니다.

다음과 같은 조건을 따라야 합니다:



저작자표시. 귀하는 원저작자를 표시하여야 합니다.



비영리. 귀하는 이 저작물을 영리 목적으로 이용할 수 없습니다.



변경금지. 귀하는 이 저작물을 개작, 변형 또는 가공할 수 없습니다.

- 귀하는, 이 저작물의 재이용이나 배포의 경우, 이 저작물에 적용된 이용허락조건을 명확하게 나타내어야 합니다.
- 저작권자로부터 별도의 허가를 받으면 이러한 조건들은 적용되지 않습니다.

저작권법에 따른 이용자의 권리는 위의 내용에 의하여 영향을 받지 않습니다.

이것은 [이용허락규약\(Legal Code\)](#)을 이해하기 쉽게 요약한 것입니다.

[Disclaimer](#)

Thesis for the Degree of Doctor of Philosophy

A Study on Robust Control System Design for Offshore Crane System based on PSO



February 2021

A Study on Robust Control System Design for Offshore Crane System based on PSO

PSO 기반 Offshore 크레인의 강인한
제어계 설계에 관한 연구

Advisor: Prof. Young-Bok Kim

by

Dong-Hun Lee

A thesis submitted in partial fulfillment of the requirements
for the degree of

Doctor of Philosophy

in Department of Mechanical System Engineering, The Graduate School
Pukyong National University

February 2021

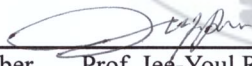
A Study on Robust Control System Design for Offshore Crane System based on PSO

A dissertation
by
Dong-Hun Lee

Approved by:



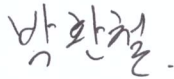
Chairman Prof. Jin-Ho Suh



Member Prof. Jee-Youl Ryu



Member Prof. Sang-Won Ji



Member Prof. Hwan-Cheol Park



Member Prof. Young-Bok Kim

February 19th 2021

Contents

Contents	i
Nomenclatures	iv
List of Figures	vii
List of Tables	xi
Abstract	xii
Chapter 1 Introduction	1
1.1 Background and Motivation.....	1
1.2 Overview of Heave Compensation.....	4
1.3 Objective of Study.....	8
1.4 Outline of Thesis.....	9
Chapter 2 Theoretical Background	13
2.1 Boundedness and Ultimate Boundedness.....	13
2.2 Particle Swarm Optimization.....	17
Chapter 3 System Description and Modeling	21
3.1 Coordinate Frame.....	21
3.2 Dynamic Modeling.....	23
3.2.1 11-DOF Kinematic Analysis.....	23
3.2.2 4-DOF Kinematic Analysis.....	28

3.2.3 Kinetic Analysis	32
3.2.4 Dynamic Decoupling with Linearization	35
Chapter 4 Controller Design	39
4.1 Control Strategy	39
4.2 Input-Output Linearization Technique based Controller Design	39
4.3 Uniformly Ultimately Bounded Controller Design	46
4.4 Integral Sliding Mode Controller Design	57
4.5 Controller Gain Optimization	61
Chapter 5 Simulation with Virtual Offshore Crane	66
5.1 Simulation Setup	66
5.2 Simulation Results	70
5.2.1 Simulation with the Nominal Model	70
5.2.2 Simulation with the Uncertain Model	73
Chapter 6 Experiment with Pilot model	78
6.1 Experimental Setup	78
6.2 Experimental Results	85
6.2.1 Experiment with the Nominal Model	85
6.2.2 Experiment with the Uncertain Model	89

Chapter 7 Conclusion and Future Study	95
7.1 Conclusion	95
7.2 Future Study	96
References	98



Nomenclatures

Variable	Description	Unit
b	Ultimate bound	-
$x_i(t)$	Position of particle i	-
$v_i(t)$	Velocity of particle i	-
C_1	Cognitive learning feature	-
C_2	Social learning feature	-
W	Inertia weight	-
o_n, x_n, y_n, z_n	North-East-Down coordinate frame	-
o_b, x_b, y_b, z_b	Body-fixed reference frame	-
\mathbf{r}_{base}^b	Vector from the origin o_b to the crane base expressed in the b-frame	-
\mathbf{r}_{boom}^b	Vector from the crane base to crane tip expressed in the b-frame	-
\mathbf{r}_{tip}^b	Vector from the origin to crane tip	-

	expressed in the b-frame	
$\mathbf{R}_b^n(\Theta)$	Rotation matrix	-
\mathbf{r}_{tip}^n	Vector from the origin o_n to the crane tip expressed in the n-frame	-
\mathbf{r}_{load}^n	Vector from the crane tip to payload position	-
l_w	Rope length	m
\mathbf{P}_{tip}^n	Position vector of the crane tip expressed in n-frame	-
\mathbf{P}_{load}^n	Position vector of the payload expressed in n-frame	-
T	Kinetic energy of the offshore crane	-
U	Potential energy of the offshore crane	-
q_i	i th state of generalized coordinates	-
f_i	i th generalized force	-
f_B	Buoyancy force	-

f_h	Hydrodynamic force	-
m	Mass of Payload	kg
C_p	Added mass coefficient of payload	-
V_p	Volume of payload	m ³
E	Elasticity modulus of rope	Pa
A_r	cross section of rope	m ²
C_D	Drag coefficient	-
A_p	Cross-section in the vertical direction of payload	m ²
ρ_w	Density of water	kg/m ³
J_w	Inertia moment of winch	kg.m ²
C_w	Damping constant of winch	Pa.s
K_w	Spring constant of winch	N/m
T_w	Torque constant of winch	-
r_w	Radius of winch drum	m

List of Figures

Figure 1-1. Relationship of international Standards(ISO) on offshore structures	2
Figure 1-2. An example of the usage of the passive heave compensation	5
Figure 1-3 General structure of the offshore crane control system (active heave compensation).....	7
Figure 1-4. Proposed control system design method for offshore crane	9
Figure 2-1. Flock of birds exhibiting swarm behavior.....	17
Figure 3-1. Notation of motion for marine crafts and reference frames.....	21
Figure 3-2. Reference frames and vector notation of offshore cranes .	24
Figure 3-3. Schematic drawing of offshore crane system.....	29
Figure 3-4. Force diagram of the payload under hydrodynamic forces	34
Figure 4-1. Control structure of the offshore crane with a input-output linearization.....	46
Figure 4-2. Control structure of the offshore crane with UUB controller	53
Figure 4-3. Controller gain optimization flow chart using PSO	65
Figure 5-1. Definition of wave encounter's angle.....	67
Figure 5-2. Heave motion RAO of vessel.....	67
Figure 5-3. Roll motion RAO of vessel	67

Figure 5-4. Desired position of the payload.....	68
Figure 5-5. Wave disturbance displacement.....	69
Figure 5-6. Payload position response without compensation controller.....	71
Figure 5-7. Payload position response with IOLC.....	71
Figure 5-8. Payload position response with UUB+IOLC.....	72
Figure 5-9. Payload position response with ISMC.....	72
Figure 5-10. Payload position error.....	73
Figure 5-11. Rope tension response.....	73
Figure 5-12. Payload position response without compensation controller.....	75
Figure 5-13. Payload position response with IOLC for uncertain model.....	75
Figure 5-14. Payload position response with UUB+IOLC for uncertain model.....	76
Figure 5-15. Payload position response with ISMC for uncertain model.....	76
Figure 5-16. Uncertain model payload position error.....	77
Figure 5-17. Rope tension response for uncertain model.....	77
Figure 6-1. Pilot offshore crane model and wave basin for experiment.....	78
Figure 6-2. The hardware configuration diagram of the control system.....	79

Figure 6-3. Comparison result between experiment and simulation result of actuator.....	80
Figure 6-4. FFT results of the pitch motion(angle, angular velocity and acceleration).....	82
Figure 6-5. FFT results of the roll motion.....	81
Figure 6-6. Payload used in experiments	83
Figure 6-7. Desired position of the payload used in experiment	84
Figure 6-8. Payload position response from the experiment without compensation controller.....	86
Figure 6-9. Payload position response from the experiment with IOLC	86
Figure 6-10. Payload position response from the experiment with UUB+IOLC	86
Figure 6-11. Payload position response from the experiment with ISMC	87
Figure 6-12. Payload position error from experiment.....	88
Figure 6-13. Rope tension response from the experiment	88
Figure 6-14. Suction pile: 3D printed model for the configuration of parametric variation.....	89
Figure 6-15. Manifold: 3D printed model for the configuration of parametric variation.....	89
Figure 6-16. 3D drawing of suction pile	90
Figure 6-17. 3D drawing of manifold	90

Figure 6-18. Example of the actual subsea installation system.....	91
Figure 6-19. Payload position response from the uncertain model experiment without compensation controller.....	92
Figure 6-20. Payload position response from the uncertain model experiment with IOLC	92
Figure 6-21. Payload position response from the uncertain model experiment with UUB+IOLC.....	93
Figure 6-22. Payload position response from the uncertain model experiment with ISMC.....	93
Figure 6-23. Payload position error from the uncertain model experiment.....	94
Figure 6-24. Rope tension response from the uncertain model experiment.....	94

List of Tables

Table 3-1. The notation of SNAME for marine vessels	23
Table 5-1 Parameters of vessel and wave used in simulation	66
Table 5-2. Parameter of offshore crane system used in simulation.....	69
Table 5-3. Optimized controller gain and the results of performance index	70
Table 5-4. Parameter variation range	74
Table 5-5. Performance index of each controller	74
Table 6-1. Experimental apparatus specification of the offshore crane model	79
Table 6-2. Wave disturbance used in the experiment.....	81
Table 6-3. Controller gain used in experiment.....	84
Table 6-4. Performance index of each wave conditions.....	85
Table 6-5. Performace index of each wave condition and payload shape.....	91

PSO 기반 Offshore 크레인의 강인한 제어계 설계 에 관한 연구

이동훈

부경대학교 대학원 기계시스템공학과

요약

심해저 개발 및 건설작업이 대두됨에 따라 해상크레인의 수요가 지속적으로 증가하고 있다. 게다가 해상크레인 세계시장 가치는 연평균 9%성장률로 증가할 것으로 내다보고 있음에 따라 관련 기술의 필요성이 강조되고 있다. 해상크레인의 주된 목적은 부하를 해저 목표지점에 안전하고 정확하게 위치시키는 것이다. 작업 종류에 따라서 부하를 수십센티 미터 범위 이내에 위치시켜야 하는 정교한 작업을 수행해야 한다.

그러나 선박에 설치되어 운용되는 크레인은 항상 파랑외란 등 해상환경의 영향을 받을 수 밖에 없으므로 정교한작업을 수행하기 어렵다. 예를 들어, 파랑의 영향으로 발생하는 선박동요로 인해 크레

인 팀의 불안정한 운동이 야기되고 부하이동작업을 어렵게 한다. 또한 부하가 수중에 잠수된 상태에서는 유체력의 작용으로 인하여 부하변동을 가중시키게 된다. 특히, 유체력에 의한 부하변동은 조류나 부하의 형상에 의존하므로 상황에 따라 부하의 운동특성도 크게 달라진다. 작업안정성을 개선하기 위하여 외적환경에 의한 영향을 정확히 파악할 수 있으면 좋으나, 지속적으로 변하는 해상환경 등으로 인해 그 영향을 파악하는 것은 사실상 불가능하다. 그러므로 해상에서의 작업은 예측할 수 없는 해상조건과 시스템 파라미터 변동 등으로 인하여 굉장히 까다롭고 위험하다. 따라서 이러한 작업환경에서도 작업안정성과 정교한 작업성을 보장할 수 있는 강인한 제어시스템 구축이 반드시 필요하다.

위와 같은 문제점을 고려하여, 본 논문에서는 파랑외란뿐만 아니라 파라미터 변동과 같은 불확실성에도 우수한 성능을 확보할 수 있는 제어계설계법을 제안한다. 구체적으로는 기 설계된 제어계에 대하여 에너지기반 리아프노프 함수를 도입하여 균일궁극유계(uniformly ultimately bounded, UUB)조건을 만족시키는 제어입력을 설계한다. 이로 인해 시스템 제어출력 및 상태가 궁극유계 이내에 존재하도록 함으로써 제어성능 개선이 보장되게 된다.

제안하는 제어계설계법을 구현하기 위하여, 입출력 선형화 제어기(input-output linearization controller, IOLC)를 적용한 해상크레인 제어시스템에 관한 사전연구결과를 이용하였다. IOLC 제어기는 제어대상에 불확실성이 존재할 경우 선형화과정이 완벽이 이루어지지 않기

때문에 강인하지 않은 것으로 잘 알려져 있다. 그러므로 본 연구에서 제어대상으로 하는 시스템과 같이 불확실성이 존재하는 경우 강인성 확보가 더욱 요구된다. 이와 같은 사실을 고려하여, 제어성능 개선을 위해 IOLC 가 적용된 제어계에 대하여 본 논문에서 제안하는 제어기설계방법을 이용하여 IOLC 와 결합한 UUB 기반 제어기 (UUB+IOLC)를 설계하였다.

설계한 제어기의 이득 최적화를 위하여 입자군집최적화(particle swarm optimization, PSO)기법을 사용하였다. 제어기 이득은 반복적인 과정을 거쳐 적절한 값을 선정하는 것이 일반적이다. 그러나 이러한 시행착오법의 경우 선정된 이득이 최상의 응답을 보장하지는 않는다. 그러므로 본 논문에서는 최적화 기법을 이용하여 제어기 이득을 최적화하여 제어계의 최적 성능 보장 및 제어기 이득 선정 어려움을 해소하였다.

본 논문에서 제안한 기법의 유효성은 시뮬레이션과 실험을 통해 확인하였다. 시뮬레이션은 실제 작업환경과 유사한 환경을 모의하였으며, 실험은 파일럿 해상크레인 모델을 이용하여 수행하였다. 특히, 실제 작업환경을 고려하여 파라미터 변동이 존재하는 경우에 대한 시뮬레이션과 실험을 각각 수행하였다. 각 결과를 통해 강인한 제어계 설계의 필요성을 보여주었을 뿐만 아니라, 제안한 제어계 설계법을 통해 불확실성에 대한 강인성 확보는 물론 제어성능까지 개선할 수 있음을 확인하였다.

1 Introduction

1.1 Background and Motivation

The offshore installation of underwater structures for oil and gas production and wind turbines is becoming more important. At the same time, the demand for a high-performance offshore crane is increasing. Hence, the construction of underwater structures with high operability is required.

However, various unpredictable disturbances and parameter variations are always impacting marine systems. The vessel moves away from the desired position both horizontally and rotationally under wave, wind, ocean current disturbance. This is the main issue of underwater installations and, in particular, crane systems since their operation is strongly affected by the vessel motion. The horizontal motion of the vessel is controlled by the vessel motion control systems, such as DPS(Dynamic Positioning System)[1]–[4]. However, the rotational motion of the vessel is completely ignored in DPS. For offshore lifting operation, the rotational motion of the vessel has a significant effect on the vertical motion of crane tip during underwater lifting operations.

The other factor affecting the operability of offshore cranes is hydrodynamic forces that cannot be directly measured nor predicted. These forces can act as an added mass or drag force of the payload, leading to undesirable load tension variation.

Therefore, the wave-induced motion of the vessel and hydrodynamic force of payload lead to a critical tension of the rope. The tension must not exceed a safety limit; otherwise, it can lead to rope failure. For this reason, the operator will have many difficulties lifting and lowering the payload.

All associates acknowledge the risk of harsh environments, and incorporated the safety measures in regulatory frameworks. There are also classification society standards that cover the design of an offshore structure, including marine cranes. For example, the standards of American Petroleum Institute(API), European Normalised Standards, International Organisation for Standardisation(ISO) are being adopted globally to enhance the operational safety of offshore structures used by the gas and oil industries.

For starters, ISO 19900(general requirements for offshore structures) constitute common basis general requirements and recommendations for designing and assessing offshore structures, which encompass both

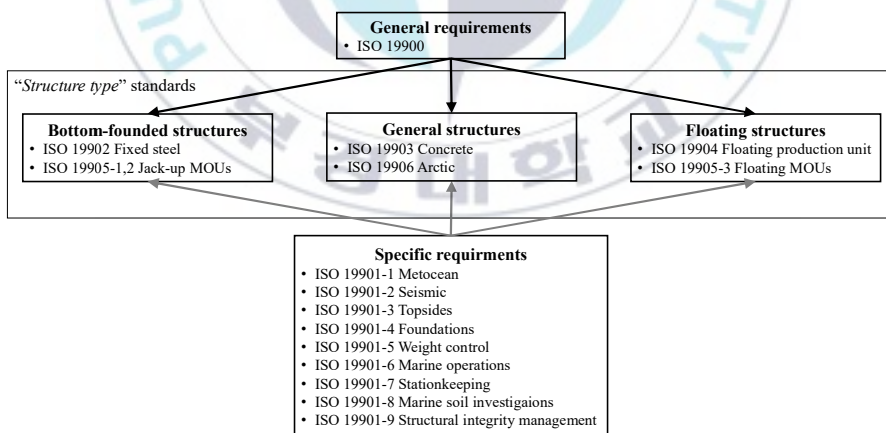


Figure 1-1. Relationship of international Standards(ISO) on offshore structures
'structure type' standards(ISO 19902, ISO 19905-1,2, ISO 19903, ISO

19906, ISO 19904 and ISO 19905-3) and specific requirements(ISO 19901) as shown in Figure 1-1.

Especially, ISO 19901-6 specifies requirements and guidance of lifting operations such that safety factors, crane vessel, underwater, heave compensated lifts and lifts using dynamic positioning.

Additionally, some standards are specifying the requirements and recommendation for marine cranes as follow

ISO

- ISO 19354 Marine cranes - General requirements
- ISO 19355 Marine cranes - Structural requirements
- ISO 19356 Marine cranes - Test specifications and procedures
- ISO 19357 Marine cranes - Design requirements for low temperature operation
- ISO 19359 Marine cranes - Design methods for drums
- ISO 19360 Marine cranes - Technical requirements for rigging applications
- ISO 21125 Marine cranes - Manufacturing requirements
- ISO 21131 Marine cranes - Noise limits and measuring method
- ISO 21132 Marine cranes - Operation and maintenance requirements

API

- API RP 2C Specification for offshore pedestal-mounted cranes
- API RP 2D Recommended practice for operation and maintenance for offshore cranes

Operators should refer to the appropriate standards for cranes used in offshore. The referenced standards should provide proper information to ensure that the crane withstands under harsh environments.

However, despite these efforts, accidents relate to offshore crane keep occurring in recent years. On 15 June 2020, Heerema's Aegir lift vessel was piling the jacket foundation piles off Taiwan's coast. During the pile driving work, the pile was dropped fall. Fortunately, there were no injuries from the incident. Only the piling frame and pin pile were damaged[5]. On 8 March 2020, Larsen & Toubro's LTS-3000 vessel was performing the installation of the jacket off India's western coast. During the lifting work, the offshore jacket was dropped fall. Unfortunately, two staff have suffered injuries during the incident[6]. These incidents lead to increasing costs and lowering efficiency. Therefore, it is necessary that a more reliable system guarantees operation to reduce production downtimes. In this thesis, to deal with such installation works with performing safety and efficiency, a payload control system is studied.

1.2 Overview of Heave compensation

It is essential to keep the payload position stable even under harsh sea conditions to improve crane operations efficiency. Decoupling the vertical payload motion from the vessel's rotational motion requires compensation systems. By using these compensation systems, the operability of the underwater lifting system under harsh sea conditions can be improved.

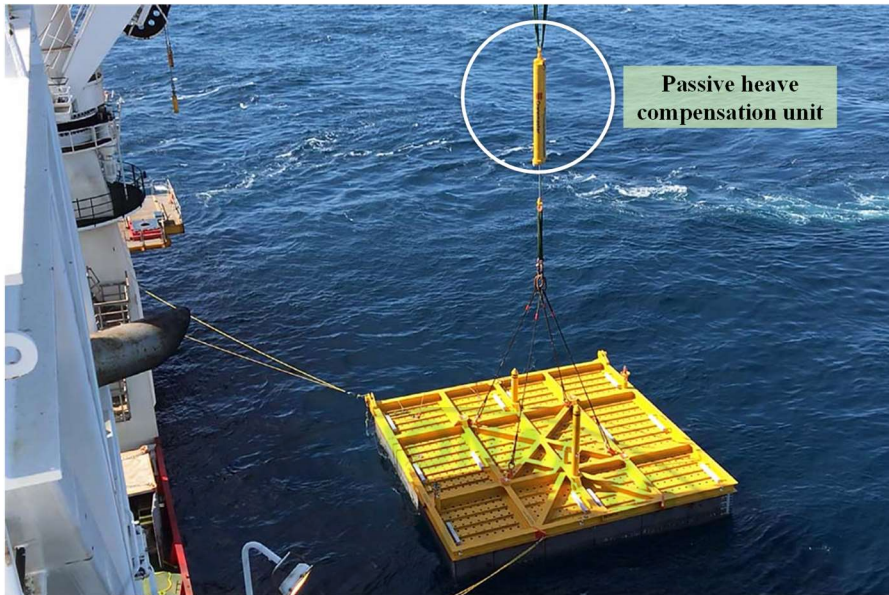


Figure 1-2. An example of the usage of the passive heave compensation

The problem of efficient and safe underwater installations in harsh sea conditions has been investigated in several previous studies. Fundamentally, there are two different types of heave compensation. The first one is the passive heave compensation (PHC). Figure 1-2 shows an example of the operation with PHC for subsea manifold installation. This system consists of a pneumatic cylinder, gas chamber, and an accumulator used to compensate for dynamic forces generated by ship motion. In [7], a performance comparison was conducted between a cage-mounted and ship-mounted PHC. Then, in [8], using a numerical optimization technique, the compensator stiffness and damping coefficient were determined in order to minimize the response.

The second one is the active heave compensation (AHC) that

compensates for the heave motion actively. At first, the position and orientation of the vessel is measured via an inertial measurement unit(IMU) or motion reference unit(MRU). This signal is transferred to an AHC control system with proper signal processing such as prediction and trajectory generation. The AHC computes the depth of the payload according to the encoder of the winch, position and orientation of the vessel. If the payload's depth does not match the target depth, the AHC sends a lowering or hoisting signal to the winch. As a result, AHC minimizes the heave motion of the suspended payload regardless of the vessel's motion in offshore installation operations. Figure 1-3 shows an example of the general control structure of the AHC[9], [10].

For example, in [11]–[15], based on linear and nonlinear control techniques, several control systems were proposed to improve the AHC. In [11]–[14], focus on not only the AHC, but also on the wave synchronization during water entry of the payload. In [11], a two-phase controller is proposed. The first-phase controller is for heave compensation, whose objective is the keeping the tension to a constant value equal to the weight of the payload. In the second-phase controller, the relative speed of the payload and sea surface is controlled in order to minimize the slamming force during water entry of payload. In [12], the authors extended this two-phase controller by an adaptive observer of the external model. In [13], [14], the feedforward control technique for the wave synchronization during the water entry of the payload was combined with feedback linear control techniques for AHC. In [15], the authors present a constructive method to design a nonlinear

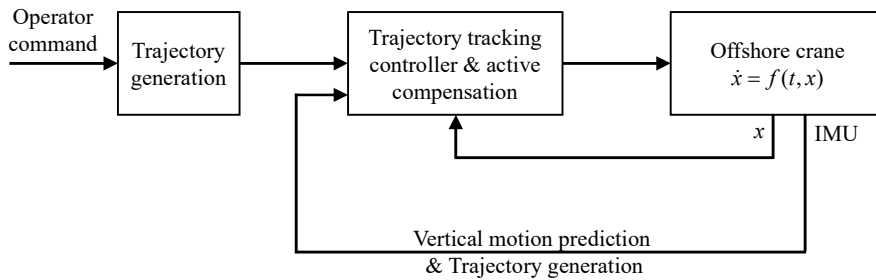


Figure 1-3 General structure of the offshore crane control system (active heave compensation)

controller. The heave velocity and the force acting between AHC unit and the riser/drill string are estimated by a disturbance observer.

However, in these papers, the rotational motion of the vessel was completely ignored. In a conventional offshore crane, the crane tip moves not only vertical motion but also rotational motions resulting from the roll and pitch motions of the host vessel. Hence, it is necessary to compensate for these rotational motions caused by the roll and pitch rotations of the vessel, thus enhancing the performance of the crane system.

In recent years, numerous publications have been concentrating on studying the load position control problems of the crane system. Thus, many control algorithms have been proposed. These control methods are summarized and categorized into two approaches: the open-loop methods [16]–[19] and the closed-loop methods [9], [10], [20], [21]. It is an open-loop control method in which [16]–[19] proposed an input-shaping control technique to investigate the dynamic behavior of the crane based on a nonlinear model. Even though the open-loop controller has shown many advantages, it is a well-known fact that it may not reduce the influence of

disturbances generated by external sources. In contrast to the open-loop control method, the output feedback control theory [20], the nonlinear tracking control [22], and the input-output linearization control [9], [10] are examples of the closed-loop control methods.

Nevertheless, the classical feedback linearization technique [23] has certain disadvantages regarding robustness. Since the system linearization is achieved by eliminating the nonlinear terms, the simplification of the nonlinear system equations can affect the robustness if the nonlinearity is uncertain [24]–[26]. Therefore, it is necessary to design a robust controller to cope with parametric variations.

1.3 Objective of Study

The main objective of this study is to suggest a control system design method for the offshore crane system to cope with disturbances and parametric variations. The main contributions of this study to achieve such an objective are summarized as follows.

- 11-DOF and 4-DOF kinematic analysis are executed. Following these kinematic models, and by decoupling the dynamics, the offshore crane decoupled dynamic model is derived.
- Lyapunov-like analysis method is used to design the proposed controller to improve the control performance and ensure the robustness of the existing control method. (see Figure 1-4)

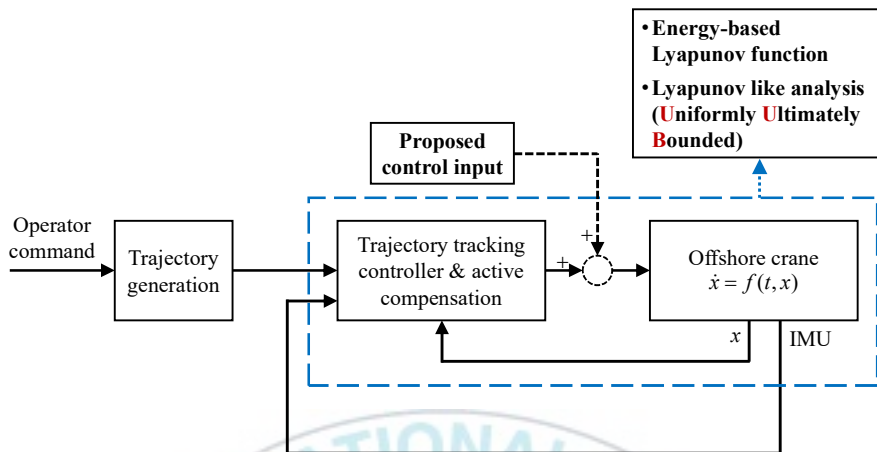


Figure 1-4. Proposed control system design method for offshore crane

- The proposed controller guarantees the uniformly ultimate bounded criterion for the proper definition of the system's output and state. This approach is intended to improve the positioning performance and suppress the rope tension regardless of wave disturbances and parametric variations. (see Figure 1-4)
- To evaluate the performance of proposed control systems, an additional robust controller is designed.
- The particle swarm optimization technique is applied to obtain the optimal controller gain.
- The control performance and the effectiveness of the proposed control systems are validated through simulation and experimental studies.

1.4 Outline of Thesis

The structure of this thesis is organized as follow

Chapter 1: Introduction

In this chapter, the background and motivation of this study are discussed. The overview of the heave compensation in terms of mechanical structure and control system are presented. And the objective of this study is given.

Chapter 2: Theoretical Background

This chapter presents a theoretical background of uniformly ultimately bounded(UUB) and particle swarm optimization(PSO). In section 2.1, the definitions of uniformly bounded and uniformly ultimately bounded are presented. and the theorem for showing the boundedness with Lyapunov-like analysis is given. In section 2.2, the background and flow chart of PSO is presented. then, pseudo code for implementing the PSO is given.

Chapter 3: System Description and Modeling

In chapter 3, the mathematical model of the offshore crane is presented. Firstly, kinematic analysis with a full dynamic(11-DOF) offshore crane is executed. By considering the real worksite, 11-DOF is reduced to 4-DOF with assumptions that emphasize the important elements and neglect the minor ones of dynamic. Using the kinematic analysis of 4-DOF model, the

nonlinear motion equation is derived with Lagrange's equation. Then, the decoupled linear model of the offshore crane is derived by decoupling the nonlinear motion equation with linearization.

Chapter 4: Controller Design

In chapter 4, three nonlinear controllers for the offshore crane is designed. Firstly, input-output linearization technique based controller, including disturbance decoupling term, is designed. Then, UUB based control system design method is proposed. In this method, a closed-loop model with input-output linearization technique based controller is used. Based on this closed-loop model, the energy-based Lyapunov function is introduced. Then, derive the controller that satisfies the UUB condition. To evaluate the performance of proposed control systems, an integral sliding mode controller is designed. The controller gain optimization procedure with PSO is introduced.

Chapter 5: Simulation with Virtual Offshore Crane

In chapter 5, the simulation with the virtual offshore crane is conducted. With the optimized controller gain, simulate with nominal model and uncertain model. Worse sea conditions than the nominal model case, and parametric variations are considered as an uncertain model. The simulation results are presented, and each controller's characteristic is carefully

considered.

Chapter 6: Experiment with the Pilot Model

In chapter 6, with the pilot model of the offshore crane, the experiment is carefully performed. Experimental apparatus are presented in detail. The experiment is performed with nominal model and uncertain model. To configure the parametric variations, two different 3D printed models of the payload are introduced. Moreover, in every experiment, worse sea conditions are configured. The experiment results are presented and the effectiveness of the proposed control system design method is validated.

Chapter 7: Conclusion and Future Study

In chapter 7, conclusions for this thesis are presented, and some ideas for future work are shown.

2 Theoretical Background

2.1 Boundedness and Ultimate Boundedness

This section will introduce the boundedness and ultimate boundedness definitions and theorems as stated in [27]. In order to show the boundedness of the state equation's solution, the Lyapunov analysis is used, even if the equilibrium point is not at the origin. Consider the system

$$\dot{x} = f(t, x) \quad (2-1)$$

where f is piecewise continuous in t , and locally Lipschitz¹.

Definition 1

- If there exists a constant $c > 0$, independent of $t_0 \geq 0$, and for every $a \in (0, c)$, there is $\beta = \beta(a) > 0$, independent of t_0 , such that

¹ Lipschitz condition[27]: If the Eq.(2-1) with $x(t_0) = x_0$ satisfies the

inequality $\|f(t, a) - f(t, b)\| \leq L \|a - b\|$ for all (t, a) and (t, b) in some neighborhood of (t_0, x_0) , the system is Lipschitz condition.

$$\|x(t_0)\| \leq a \Rightarrow \|x(t)\| \leq \beta, \quad \forall t \geq t_0$$

(2-2)

then, the solutions of the system (2-1) are uniformly bounded.

- If (2-2) holds for an arbitrarily large a , the solutions of the system (2-1) are globally uniformly bounded.
- If there exists a constant $b > 0$ and $c > 0$ independent of $t_0 \geq 0$, and for every $a \in (0, c)$, there is a $T = T(a, b) \geq 0$ independent of t_0 , such that

$$\|x(t_0)\| \leq a \Rightarrow \|x(t)\| \leq b, \quad \forall t \geq t_0 + T \quad (2-3)$$

then, the solutions of the system (2-1) are uniformly ultimately bounded with b as the ultimate bound.

- If (2-3) holds for an arbitrarily large a , the solutions of the system (2-1) are globally uniformly ultimately bounded.

In order to show how the Lyapunov-like analysis can be utilized for boundedness and ultimate boundedness, let us consider the positive definite function $V(t, x)$ which is continuously differentiable.

Theorem 1

Consider the continuously differentiable function $V(t, x)$, such that

$$\alpha_1(\|x\|) \leq V(t, x) \leq \alpha_2(\|x\|) \quad (2-4)$$

$$\frac{\partial V}{\partial t} + \frac{\partial V}{\partial x} f(t, x) \leq -M(x), \quad \forall \|x\| \geq \mu > 0, \forall t \geq 0 \quad (2-5)$$

where α_1 and α_2 are class \mathbf{K}^2 functions, and $M(x)$ is a continuous positive definite function. We define $\tau > 0$, such that

$$\Omega < \alpha_2^{-1}(\alpha_1(\tau)) \quad (2-6)$$

Then, there exists a class \mathbf{KL}^3 function β satisfying $\|x(t_0)\| \leq \alpha_2^{-1}(\alpha_1(r))$, for every initial state $x(t_0)$. We define a $T \geq 0$ such that the solution of the system (2-1) satisfies the following

² Class kappa(Class \mathbf{K}): If continuous function α is strictly increasing $\alpha : [0, a) \rightarrow [0, \infty)$ and $\alpha(0) = 0$, it is class kappa.

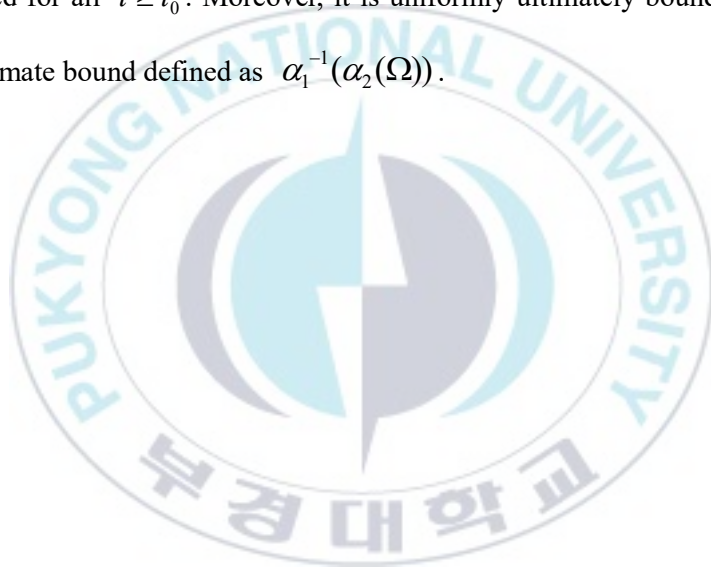
³ Class kappa-l(Class \mathbf{KL}): For each fixed s , the function $\beta(r, s)$ belongs to class kappa

For each fixed r , the function $\beta(r, s)$ is decreasing with respect to s and $\beta(r, s) \rightarrow 0$ for $s \rightarrow \infty$.

$$\|x(t)\| \leq \beta(\|x(t_0)\|, t - t_0), \quad \forall t_0 \leq t \leq t_0 + T \quad (2-7)$$

$$\|x(t)\| \leq \alpha_1^{-1}(\alpha_2(\Omega)), \quad \forall t \geq t_0 + T \quad (2-8)$$

Then, the inequalities (2-7) and (2-8) imply that $x(t)$ is uniformly bounded for all $t \geq t_0$. Moreover, it is uniformly ultimately bounded with the ultimate bound defined as $\alpha_1^{-1}(\alpha_2(\Omega))$.



2.2 Particle Swarm Optimization

Particle swarm optimization (PSO) is a population-based evolutionary optimization technique developed by Kennedy and Eberhart in 1995 [28], [29]. PSO is inspired by the social behavior of fish schooling or bird flocking as shown in Figure 2-1[30].

PSO is an evolutionary computation technique similar to a genetic algorithm (GA) in terms of initializing the system with a population of random solutions. However, PSO differs from GA in terms of assigning to each randomized velocity a potential solution. Furthermore, these potential solutions (particles) are flown through the problem space.

The advantages of the PSO are its stable convergence performance and its relatively simple implementation. PSO is proved to be efficient and



Figure 2-1. Flock of birds exhibiting swarm behavior

powerful in solving complex problems such as nonlinearity and non-differentiability, as well as high dimensionality and multiple optima.

In the problem space, the coordinates of each particle that keeps track are associated with the best solution. We define this value as ‘pbest’, which is the personal best position of the i th particle and ‘gbest’ is the position of the overall best particle. At each time step, the position $x_i(t)$ and velocity $v_i(t)$ of particle i are led toward its pbest and gbest locations. Mathematically, the particles are updated based on the following equations.

$$x_i(t+1) = x_i(t) + v_i(t+1) \quad (2-9)$$

$$v_i(t+1) = Wv_i(t) + C_1r_1(x_{pbest_i} - x_i(t)) + C_2r_2(x_{gbest} - x_i(t)) \quad (2-10)$$

where C_1 is the cognitive learning feature and which represents the attraction of a particle to its own success. C_2 is the social learning factor and it represents the attraction that a particle has toward the success of its neighbors. W is the inertia weight and controls the influence of the previous velocity on the current velocity. Using these mathematical equations, the process of implementing the PSO is as follow;

Step 1 Initialize a population of particles (n dimension) and velocities with a random position in the problem space. The dimension is the same

as the size of the parameter to optimize.

Step 2 For each particle, calculate the desired optimization performance index.

Step 3 Compare the performance index of each particle with its pbest. Set the pbest value to the i th (current) value, if the i th value is better than pbest. And the pbest location becomes the i th location.

Step 4 Compare the performance index results with the overall previous best. If the i th value is better than gbest, reset the gbest to the value of the i th particle.

Step 5 Update the velocity and position of the particle along with Eq.(2-9) and Eq.(2-10).

Step 6 Repeat step.2 to step.5 until a criterion is satisfied.

Usually, the stopping criterion can be set as the maximum number of iterations, minimum gbest gradient of a performance index, desired gbest value, or others.

The pseudo code of the procedure is as follows[31]

For each particle

 Initialize particle

END

Do

 For each particle

Calculate fitness value

If the fitness value is better than the best fitness value (pBest) in history

set current value as the new pBest

End

Choose the particle with the best fitness value of all the particles as the gBest

For each particle

Calculate particle velocity according equation (a)

Update particle position according equation (b)

End

While maximum iterations or minimum error criteria is not attained

3 System Description and Modeling

3.1 Coordinate Frame

When describing marine craft motion, it is necessary to define the reference frame. In this study, two geographic reference frames are introduced as illustrated in Figure 3-1.

North-East-Down (NED) coordinate frame

The NED coordinate system (n-frame, $\{n\} = (o_n, x_n, y_n, z_n)$) is relative to the Earth's reference. The n-frame is defined as the tangent of the Earth's surface moving along with the marine crafts. The positive direction of x_n -axis points towards the ellipsoid North, y_n -axis points towards ellipsoid East, and the z_n -axis points towards the center of the Earth. Using the concept of the flat-Earth model and assuming that the n-frame is an

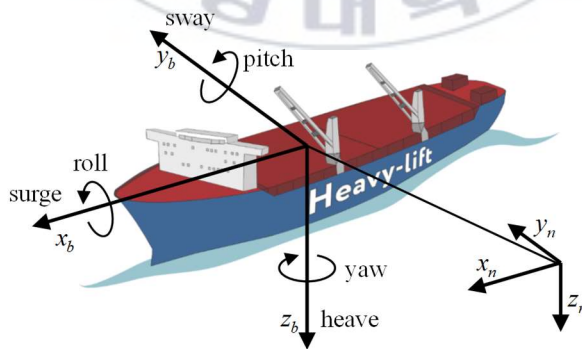


Figure 3-1. Notation of motion for marine crafts and reference frames

inertial reference frame for marine crafts, it allows for Newton's law to be applied.

Body-Fixed reference frame

The Body-Fixed reference frame (b-frame, $\{b\} = (o_b, x_b, y_b, z_b)$) is a moving coordinate frame fixed to the marine craft. The origin o_b is usually chosen to coincide with the center of mass of the marine vessel. The positive direction of the x_b -axis points towards the bow (longitudinal axis), the y_b -axis points towards the starboard (transverse axis), and the z_b -axis points downward (from top to bottom). While the angular and linear velocities of the marine craft should be defined in the b-frame, the position and orientation of the marine vessel are defined in the inertial reference frame (the n-frame).

As shown in Figure 3-1, the marine craft is moving in 6-DOF. Thus, six independent coordinates are needed to describe the position and orientation of the marine vessel. The first three coordinates correspond to the translational displacement along the x , y , and z axes. The last three coordinates are rotational motions and are used to define the orientation. For marine crafts, the six motion components are independent of each other, and they are defined by the SNAME (Society of Naval Architects & Marine Engineers, 1950) as shown in Table 3-1.

Table 3-1. The notation of SNAME for marine vessels

	DOF	Linear and angular velocities	Position and Euler angles
1	motion in the x direction (surge)	u	x
2	motion in the y direction (sway)	v	y
3	motion in the z direction (heave)	w	z
4	rotation about the x -axis (roll)	p	φ
5	rotation about the y -axis (pitch)	q	θ
6	rotation about the z -axis (yaw)	r	ψ

3.2 Dynamic Modeling

As mentioned in chapter 1, in this study, the objective is to design a payload position control system for offshore cranes. An offshore crane, especially the boom crane system, has 11-DOF in total. That is, the crane has 5-DOF itself, 2-D swing angle of the payload, luff/slew angle of the boom, and the cable length.

In this study, a kinetic analysis with the 11-DOF dynamic system will be conducted. Subsequently, after careful consideration of the operating environment, the kinetic analysis will be conducted with a reduced-dimension system.

3.2.1 11-DOF Kinematic Analysis

It is assumed that the position (n-frame) and the angular and linear velocities (b-frame) of the offshore crane are known and defined as in Figure

3-2. Additionally, it is assumed that the origin of the b-frame coincides with the center of mass of the offshore crane.

The position and attitude of the offshore crane expressed in the n-frame are defined as

$$\mathbf{p}^n = [x \quad y \quad z]^T, \quad \Theta = [\varphi \quad \theta \quad \psi]^T \quad (3-1)$$

The linear and angular velocities of the offshore crane expressed in the b-frame are defined as

$$\mathbf{v}_o^b = [u \quad v \quad w]^T, \quad \boldsymbol{\omega}_o^b = [p \quad q \quad r]^T \quad (3-2)$$

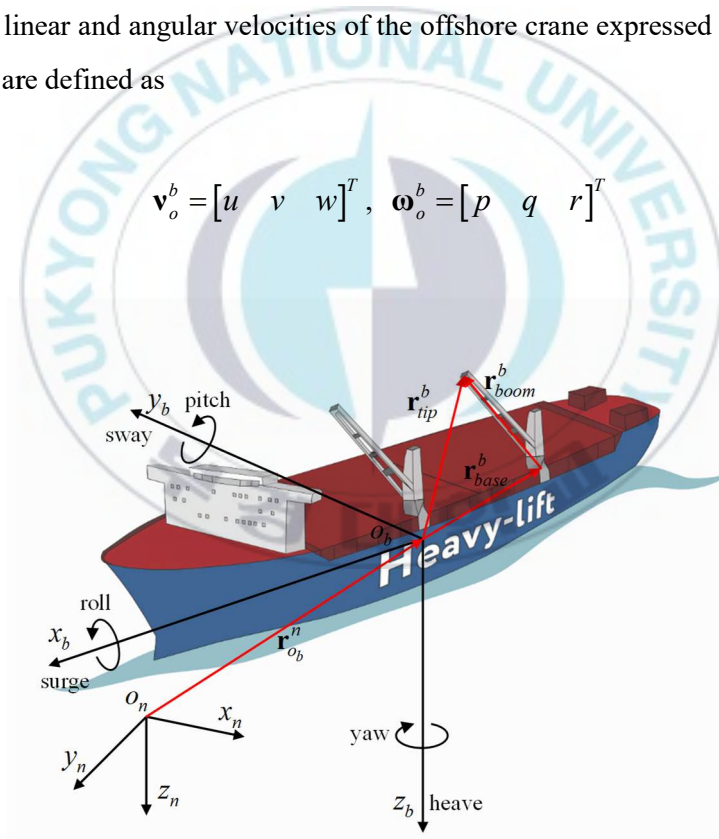


Figure 3-2. Reference frames and vector notation of offshore cranes

Using a vector from the origin o_b to the crane base expressed in the b-frame (\mathbf{r}_{base}^b) and a vector from the crane base to the crane tip expressed in the b-frame (\mathbf{r}_{boom}^b), the resultant vector from the origin to the crane tip (\mathbf{r}_{tip}^b) can be determined as follows

$$\mathbf{r}_{tip}^b = \mathbf{r}_{base}^b + \mathbf{r}_{boom}^b = \begin{bmatrix} x_{tip}^b & y_{tip}^b & z_{tip}^b \end{bmatrix}^T \quad (3-3)$$

In order to calculate the position, velocity, and acceleration of the crane tip in the n-frame, the rotation matrix should be introduced. The rotation matrix $\mathbf{R}_b^n(\Theta)$ from the b-frame to the n-frame is defined as $\mathbf{R}_b^n(\Theta) = \mathbf{R}_{z,\psi} \mathbf{R}_{y,\theta} \mathbf{R}_{x,\varphi}$ with each matrix is given as

$$\mathbf{R}_{z,\psi} = \begin{bmatrix} c\varphi & -s\varphi & 0 \\ s\varphi & c\varphi & 0 \\ 0 & 0 & 1 \end{bmatrix}, \quad \mathbf{R}_{y,\theta} = \begin{bmatrix} c\varphi & 0 & s\varphi \\ 0 & 1 & 0 \\ -s\varphi & 0 & c\varphi \end{bmatrix},$$

$$\mathbf{R}_{x,\varphi} = \begin{bmatrix} 1 & 0 & 0 \\ 0 & c\varphi & -s\varphi \\ 0 & s\varphi & c\varphi \end{bmatrix} \quad (3-4)$$

where $c = \cos(\cdot)$ and $s = \sin(\cdot)$. Then, the rotation matrix becomes,

$$\mathbf{R}_b^n(\Theta) = \begin{bmatrix} c\psi c\theta & -s\psi c\theta + c\psi s\theta s\varphi & s\psi s\theta + c\psi c\theta s\varphi \\ s\psi c\theta & c\psi c\theta + s\psi s\theta s\varphi & -c\psi s\theta + s\psi c\theta s\varphi \\ -s\theta & c\theta s\varphi & c\theta c\varphi \end{bmatrix} \quad (3-5)$$

The vector from the origin o_n to the crane tip expressed in the n-frame (\mathbf{r}_{tip}^n) is described as

$$\mathbf{r}_{tip}^n = \mathbf{R}_b^n \mathbf{r}_{tip}^b \quad (3-6)$$

where $\mathbf{r}_{tip}^n = [x_{tip}^n \ y_{tip}^n \ z_{tip}^n]^T$. Then, the position of the crane tip expressed in the n-frame can be described as

$$\begin{aligned} \mathbf{p}_{tip}^n &= \mathbf{r}_{o_b}^n + \mathbf{R}_b^n \mathbf{r}_{tip}^b \\ &= \mathbf{r}_{o_b}^n + \mathbf{r}_{tip}^n \end{aligned} \quad (3-7)$$

where $\mathbf{r}_{o_b}^n = [x_{o_b}^n \ y_{o_b}^n \ z_{o_b}^n]^T$. Assuming knowledge of the linear and angular velocity of the offshore crane expressed in the b-frame, the velocity of the crane tip expressed in the n-frame is described as

$$\dot{\mathbf{p}}_{tip}^n = \mathbf{R}_b^n \mathbf{v}_{tip}^b \quad (3-8)$$

where \mathbf{v}_{tip}^b is described by the cross product of $\boldsymbol{\omega}_{nb}^b \times \mathbf{r}_{tip}^b$, which results in

$$\begin{aligned}\mathbf{v}_{tip}^b &= \mathbf{v}_{o_b}^b + \boldsymbol{\omega}_{nb}^b \times \mathbf{r}_{tip}^b \\ &= \mathbf{v}_{o_b}^b + S(\boldsymbol{\omega}_{nb}^b) \mathbf{r}_{tip}^b\end{aligned}\quad (3-9)$$

where $S(\cdot)$ is the cross-product operator, $S(\boldsymbol{\omega}_{nb}^b)$ is thus defined as

$$S(\boldsymbol{\omega}_{nb}^b) = \begin{bmatrix} 0 & -r & q \\ r & 0 & -p \\ -q & p & 0 \end{bmatrix}\quad (3-10)$$

Moreover, the time derivative of the rotation matrix (\mathbf{R}_b^n) is given by [32]

$$\dot{\mathbf{R}}_b^n = \mathbf{R}_b^n S(\boldsymbol{\omega}_{nb}^b)\quad (3-11)$$

The same procedure is used to derive the acceleration of the crane tip expressed in the n-frame. Differentiating the Eq.(3-9) and using Eq.(3-11), the acceleration of the crane tip express in the n-frame is obtained as the following

$$\begin{aligned}
\ddot{\mathbf{P}}_{tip}^n &= \dot{\mathbf{R}}_b^n \mathbf{v}_{tip}^b + \mathbf{R}_b^n \dot{\mathbf{v}}_{tip}^b \\
&= \mathbf{R}_b^n S(\boldsymbol{\omega}_{nb}^n) (\mathbf{v}_{o_b}^b + S(\boldsymbol{\omega}_{nb}^n) \mathbf{r}_{tip}^b) + \mathbf{R}_{nb}^b (\dot{\mathbf{v}}_{o_b}^b + S(\dot{\boldsymbol{\omega}}_{nb}^n) \mathbf{r}_{tip}^b + S(\boldsymbol{\omega}_{nb}^n) \dot{\mathbf{r}}_{tip}^b) \quad (3-12) \\
&= \mathbf{R}_b^n \{ (S^2(\boldsymbol{\omega}_{nb}^n) + S(\dot{\boldsymbol{\omega}}_{nb}^n)) \mathbf{r}_{tip}^b + S(\boldsymbol{\omega}_{nb}^n) (\mathbf{v}_{o_b}^b + \dot{\mathbf{r}}_{tip}^b) + \dot{\mathbf{v}}_{o_b}^b \}
\end{aligned}$$

3.2.2 4-DOF Kinematic Analysis

As discussed in the previous chapter, the 11-DOF full dynamic system is too complex to describe the motion equation and design the controller. Therefore, it is necessary to simplify the system dynamics. Simplifying assumptions are introduced to emphasize the important elements and neglect the minor ones.

The reduced dimension offshore crane is modeled with the following assumptions.

- The surge, sway motion, and the yaw angle can be neglected since their amplitudes are too small due to the DPS (Dynamic Positioning System).
- The luff and slew angles are not controlled in the payload positioning task, and their values are considered constant and known.
- The crane base and the tip are aligned with the y (or x) axis of the b-frame.

As a result of the second and third assumptions, the swing motion of the payload is considered a 1-D motion. In other words, the dominant excitation

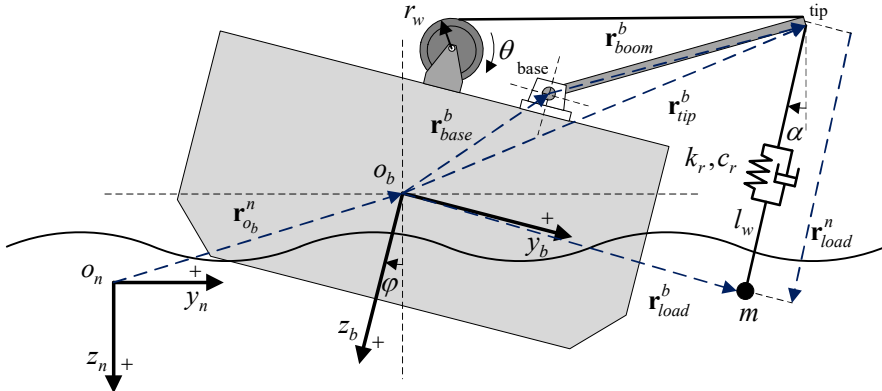


Figure 3-3. Schematic drawing of offshore crane system

of payload motion is the rotational movement around the x -axis (or y -axis) of the offshore crane.

Then, we move on to determine the movement of the offshore crane in the xz -plane (or yz -plane). The heave and roll (or pitch) motions of the offshore crane, as well as the cable length, are parameters taken into consideration. The schematic drawing of the offshore crane system used in this study is illustrated in Figure 3-3.

Following the same procedure as in section 3.2.1, we can derive the crane tip motion equation. Additionally, the payload motion equation will also be derived to further analyze the dynamics of the system.

Along with Eq.(3-3), the vector from the origin to the crane tip expressed in the b-frame is $\mathbf{r}_{tip}^b = [0 \quad y_{tip}^b \quad z_{tip}^b]^T$. As shown in Figure 3-3, since the only rotational motion considered is the one around x -axis (rolling), the rotational matrix from the b-frame to the n-frame becomes $\mathbf{R}_b^n(\boldsymbol{\Theta}) = \mathbf{R}_{x,\varphi}$. Along with this result and Eq.(3-7), the position of the crane

tip expressed in the n-frame is given by

$$\begin{aligned}
 \mathbf{p}_{tip}^n &= \mathbf{r}_{o_b}^n + \mathbf{R}_b^n \mathbf{r}_{tip}^b \\
 &= \mathbf{r}_{o_b}^n + \mathbf{r}_{tip}^n \tag{3-13} \\
 &= \begin{bmatrix} 0 \\ y_{tip}^b \mathbf{c} \varphi - z_{tip}^b \mathbf{s} \varphi \\ z_{tip}^b \mathbf{c} \varphi + y_{tip}^b \mathbf{s} \varphi + Z_{heave} \end{bmatrix}
 \end{aligned}$$

where $\mathbf{r}_{o_b}^n = [0 \ 0 \ Z_{heave}]^T$. Besides, the vector from the crane tip to the payload position is defined as

$$\mathbf{r}_{load}^n = [0 \ -(l_w + \delta) \mathbf{s} \alpha \ (l_w + \delta) \mathbf{c} \alpha]^T \tag{3-14}$$

where $l_w = l_w(0) + r_w \theta$ is the rope length and δ is the rope length variation. Then, the payload position expressed in the n-frame is given as

$$\begin{aligned}
 \mathbf{p}_{load}^n &= \mathbf{p}_{tip}^n + \mathbf{r}_{load}^n \\
 &= \begin{bmatrix} 0 \\ -(l_w + \delta) \mathbf{s} \alpha + y_{tip}^b \mathbf{c} \varphi - z_{tip}^b \mathbf{s} \varphi \\ (l_w + \delta) \mathbf{c} \alpha + z_{tip}^b \mathbf{c} \varphi + y_{tip}^b \mathbf{s} \varphi + Z_{heave} \end{bmatrix} \tag{3-15}
 \end{aligned}$$

In a similar approach, Eqs.(3-8)~(3-15) are used to derive the velocity and acceleration of the payload. The resulting velocity and acceleration

expressions of the crane tip and the payload are given as

$$\dot{\mathbf{p}}_{tip}^n = \begin{bmatrix} 0 \\ -y_{tip}^b s \varphi \dot{\varphi} - z_{tip}^b c \varphi \dot{\varphi} \\ y_{tip}^b s \varphi \dot{\varphi} - z_{tip}^b c \varphi \dot{\varphi} + \dot{Z}_{heave} \end{bmatrix} \quad (3-16)$$

$$\dot{\mathbf{p}}_{load}^n = \begin{bmatrix} 0 \\ -s \alpha (\dot{\delta} + \dot{l}_w) - c \varphi z_{tip}^b \dot{\varphi} - c \alpha (\delta + l_w) \dot{\alpha} - s \varphi y_{tip}^b \dot{\varphi} \\ c \alpha (\dot{\delta} + \dot{l}_w) + c \varphi y_{tip}^b \dot{\varphi} - s \varphi z_{tip}^b \dot{\varphi} - s \alpha (\delta + l_w) \dot{\alpha} + \dot{Z}_{heave} \end{bmatrix} \quad (3-17)$$

$$\ddot{\mathbf{p}}_{tip}^n = \begin{bmatrix} 0 \\ -c \varphi y_{tip}^b \dot{\varphi}^2 + s \varphi z_{tip}^b \dot{\varphi}^2 - c \varphi z_{tip}^b \ddot{\varphi} - s \varphi y_{tip}^b \ddot{\varphi} \\ -c \varphi z_{tip}^b \dot{\varphi}^2 - s \varphi y_{tip}^b \dot{\varphi}^2 + c \varphi y_{tip}^b \ddot{\varphi} - s \varphi z_{tip}^b \ddot{\varphi} + \ddot{Z}_{heave} \end{bmatrix} \quad (3-18)$$

$$\ddot{\mathbf{p}}_{load}^n = \begin{bmatrix} 0 \\ -s \alpha (\ddot{\delta} + \ddot{l}_w) - 2c \alpha \dot{\alpha} (\dot{\delta} + \dot{l}_w) - c \varphi y_{tip}^b \dot{\varphi}^2 + s \varphi z_{tip}^b \dot{\varphi}^2 \dots \\ -c \varphi z_{tip}^b \ddot{\varphi} + s \alpha (\delta + l_w) \dot{\alpha}^2 - c \alpha (\delta + l_w) \ddot{\alpha} - s \varphi y_{tip}^b \ddot{\varphi} \\ c \alpha (\ddot{\delta} + \ddot{l}_w) - 2s \alpha \dot{\alpha} (\dot{\delta} + \dot{l}_w) - c \varphi z_{tip}^b \dot{\varphi}^2 - c \alpha (\delta + l_w) \dot{\alpha}^2 \dots \\ -s \varphi y_{tip}^b \dot{\varphi}^2 + c \varphi y_{tip}^b \ddot{\varphi} - s \varphi z_{tip}^b \ddot{\varphi} - s \alpha (\delta + l_w) \ddot{\alpha} + \ddot{Z}_{heave} \end{bmatrix} \quad (3-19)$$

3.2.3 Kinetic Analysis

In this section, Lagrange's equation [33] is employed to derive the dynamical model of the 4-DOF offshore crane system based on the results mentioned above.

As shown in Figure 3-3, the offshore crane under consideration consists of a winch and rope suspended the payload. The following simplifying assumptions are made to render the system modeling more tractable.

- The offshore crane structure is considered a rigid body [9], [10], [34].
- The payload is considered a point mass [35], [36].
- The mass of the suspension rope of the offshore crane is massless, which implies that the cable does not bend following the crane motion [35].

The rope can be approximated by a mass-spring-damper system with the payload mass m , spring constant k_r , damping constant c_r , and the rope length variation δ . However, since the dominant damping force acting on the submerged payload is the hydrodynamic force. The rope damping force is neglected.

Based on Eqs.(3-13)~(3-17), the kinetic energy (T) and potential energy (U) of the crane tip and payload, respectively, are obtained as follows [37], [38]

$$T = \frac{1}{2} \left(m_{tip} \dot{\mathbf{p}}_{tip}^{n T} \dot{\mathbf{p}}_{tip}^n + m \dot{\mathbf{p}}_{load}^{n T} \dot{\mathbf{p}}_{load}^n \right) \quad (3-20)$$

$$U = -g \left(m_{tip} \mathbf{p}_{tip}^n + m \mathbf{p}_{load}^n \right) + \frac{1}{2} k_r \delta^2 \quad (3-21)$$

Defining the state $\mathbf{q} = [q_1 \ q_2]^T = [\delta \ \alpha]^T$ as the generalized coordinates corresponding to the generalized forces f_i . These generalized forces are given as

$$f_1 = f_B \cos \alpha + f_h(p_{load,y}^n) \sin \alpha + f_h(p_{load,z}^n) \cos \alpha \quad (3-22)$$

$$f_2 = f_B \sin \alpha + f_h(p_{load,y}^n) \cos \alpha + f_h(p_{load,z}^n) \sin \alpha \quad (3-23)$$

where Eq.(3-22) and (3-23) are the hydrodynamic forces affecting the payload in the fluid. f_B is the buoyancy force and f_h is the added mass

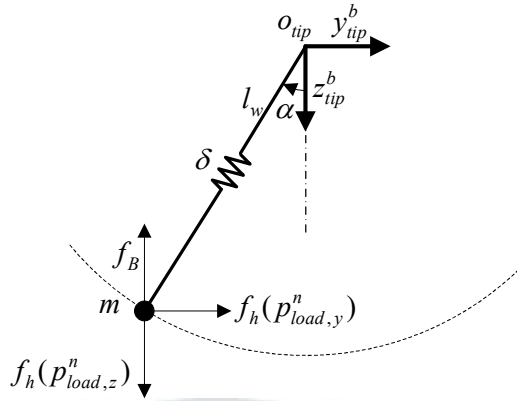


Figure 3-4. Force diagram of the payload under hydrodynamic forces and damping force as a function of the velocity and acceleration. The schematic diagram of the payload rotating about the crane tip is shown in Figure 3-4[39]. Detailed hydrodynamics are introduced in the next section. Therefore, the dynamic equation of motion can be derived from Lagrange's equation as the following

$$\frac{d}{dt} \left(\frac{\partial T}{\partial \dot{q}_i} \right) - \frac{\partial T}{\partial q_i} + \frac{\partial U}{\partial q_i} = f_i, \quad (i=1,2) \quad (3-24)$$

The resulting motion equation of the payload is derived as follows

$$\begin{aligned} & \delta k_{eq} + \ddot{\delta} m + \ddot{l}_w m - \delta \dot{\alpha}^2 m + \ddot{Z}_{heave} m c \alpha - g m c \alpha \\ & - \dot{\alpha}^2 l_w m + \dot{\varphi}^2 m y_{tip}^b s(\alpha - \varphi) + \ddot{\varphi} m y_{tip}^b c(\alpha - \varphi) \\ & + \ddot{\varphi} m z_{tip}^b s(\alpha - \varphi) - \dot{\varphi}^2 m z_{tip}^b c(\alpha - \varphi) = f_1 \end{aligned} \quad (3-25)$$

$$\begin{aligned}
& \{m(\delta + l_w)^2\} \ddot{\alpha} + 2\dot{\alpha} \dot{l}_w m + 2\dot{\alpha} \dot{l}_w l_w m - \delta \ddot{Z}_{heave} m \alpha \\
& - \ddot{Z}_{heave} l_w m s \alpha + \delta g m s \alpha + g l_w m s \alpha + 2\delta \dot{\alpha} \dot{\delta} m + 2\delta \dot{\alpha} \dot{l}_w m \\
& + \delta \dot{\varphi} m z_{tip}^b c(\alpha - \varphi) + \ddot{\varphi} l_w m z_{tip}^b c(\alpha - \varphi) - \delta \dot{\varphi} m y_{tip}^b s(\alpha - \varphi) \quad (3-26) \\
& - \ddot{\varphi} l_w m y_{tip}^b s(\alpha - \varphi) + \delta \dot{\varphi}^2 m y_{tip}^b c(\alpha - \varphi) + \dot{\varphi}^2 l_w m y_{tip}^b c(\alpha - \varphi) \\
& + \delta \dot{\varphi}^2 m z_{tip}^b s(\alpha - \varphi) + \dot{\varphi}^2 l_w m z_{tip}^b s(\alpha - \varphi) = f_2
\end{aligned}$$

3.2.4 Dynamic Decoupling with Linearization

As above-mentioned, the objective of this study is the payload positioning control problem of offshore cranes as in subsea cranes and ROV launch systems. Considering this issue, the suppression of the payload's swing motion is not a significant concern in a practical case. Therefore, decoupling the vertical motion dynamic from the swing motion dynamic is possible. In order to achieve this decoupling, various techniques were used to approach this issue. In [40], a decoupler matrix is used to cancel the input couplings. While in [41], a pseudo linear composite system is used to decouple the nonlinear coupled system into a number of independent pseudo linear SISO systems online. In this study, the small angle approximation method will be used for a more convenient design of the control system and to get more insight into the dynamics of the system.

If we consider that the payload is perturbed around the target position, the rope length is assumed to be $l_w \approx l_w(0)$, then $\dot{l}_w \approx r_w \dot{\theta}$ and $\ddot{l}_w \approx r_w \ddot{\theta}$. And using the small-angle approximation, we can get a decoupled model from the coupled nonlinear model in Eq.(3-25) and (3-26) as follow

$$\delta k_r + \delta \ddot{m} + \ddot{l}_w m + \ddot{Z}_{heave} m - gm + \ddot{\phi} m y_{tip}^b = f_B + f_h(p_{load,z}^n) \quad (3-27)$$

$$m l_w(0)^2 + g l_w(0) m \ddot{\alpha} + \ddot{\phi} l_w(0) m z_{tip}^b = f_h(p_{load,y}^n) \quad (3-28)$$

where f_B and f_h are defined as [11], [14], [34], [42]

$$f_B = -\rho_w g V_p \quad (3-29)$$

$$f_h(X) = -\rho_w V_p \ddot{X} - m_a \ddot{X} - \frac{1}{2} \rho_w C_D A_p \dot{X} |\dot{X}| \quad (3-30)$$

where ρ_w is the density of water, m_a is the added mass of the load as a function of submergence, C_D is the drag coefficient, A_p is the payload's nominal cross-section in the vertical direction. The added mass can be defined as $m_a = \rho_w V_p C_a$, where C_a is the coefficient of the added mass and depends on the shape of the payload.

Using the obtained coupled nonlinear and decoupled models, simulating each dynamical system, and analyzing the simulation's result helps to evaluate the usefulness of the decoupled model. Thus, the usefulness of the decoupled model is effectively verified through simulation and result evaluation; the reader is referred to [43]. Hence, in this study, the vertical

dynamics of the decoupled model Eq.(3-27) of the offshore crane model is used to design the control system. Combining Eq.(3-27), (3-29) and (3-30), the offshore crane model is given as

$$\begin{aligned} \ddot{\delta} m_p = & -r_w \ddot{\theta} m_p - \delta k_r + F_g - F_b \dots \\ & - \frac{1}{2} \rho_w C_D A_p \dot{p}_{load,z}^n \left| \dot{p}_{load,z}^n \right| - m_p (\ddot{Z}_{heave} + y_{tip}^b \ddot{\phi}) \end{aligned} \quad (3-31)$$

where $m_p = m + m_a + \rho_w V_p$, $F_g = gm$, $F_b = \rho_w g V_p$. The velocity of the payload about z_n -axis is $\dot{p}_{load,z}^n = r_w \dot{\theta} + \dot{\delta} + y_{tip}^b \dot{\phi} + \dot{Z}_{heave}$. In [44], the rope parameter depends on the rope length as shown in the following equation

$$k_r = \frac{EA}{l_w} \quad (3-32)$$

where E is the modulus of elasticity, A is the cross-section area of the rope.

The actuator of the offshore crane is an electric (or hydraulic) winch. A second-order differential equation is chosen to express the system dynamics of the winch.

$$J_w \ddot{\theta} + C_w \dot{\theta} + K_w \theta = T_w u_w \quad (3-33)$$

where J_w is the inertia moment, C_w is the damping constant, K_w is the stiffness constant, T_w is the torque constant, u_w is the control input.



4 Controller Design

4.1 Control Strategy

The objective of this section is to design a control system for payload position keeping under wave disturbances and parametric variations. Therefore, the primary control objective is to devise a controller such that the position of the payload $P_{load,z}^n$ converges to its desired position P_{ref}^n , generated by the operator, regardless of the motion of the vessel and the variations of the wire rope. In this case, the winch should compensate for the movement of the vessel and variations of the rope and track the P_{ref}^n to achieve the aforementioned control objective.

4.2 Input-Output Linearization Technique based Controller Design

In order to design the controller with the input-output linearization technique, the dynamic model of the system Eq.(3-27) should be represented as a state space model. The linearized payload position from Eq.(3-15) and the state are given as

$$p_{load,z}^n = l_w(0) + r_w \theta + \delta + z_{tip}^b + y_{tip}^b \varphi + Z_{heave} \quad (4-1)$$

$$\begin{aligned}\mathbf{x} &= [x_1 \quad x_2 \quad x_3 \quad x_4 \quad x_5 \quad x_6]^T \\ &= [\delta \quad \dot{\delta} \quad \theta \quad \dot{\theta} \quad \lambda \quad \dot{\lambda}]^T\end{aligned}\quad (4-2)$$

where the $\lambda = Z_{heave} + y_{tip}^b \varphi$ is the displacement along the z_n -axis of the crane tip created by the vessel motion. Along with Eq.(3-31) and (3-33), the dynamic model of the offshore crane is given by

$$\begin{aligned}\dot{\mathbf{x}} &= \mathbf{f}(\mathbf{x}) + \mathbf{g}(\mathbf{x})u + \mathbf{p}(\mathbf{x})d \\ y &= h(\mathbf{x})\end{aligned}\quad (4-3)$$

$$\mathbf{f}(\mathbf{x}) = \begin{bmatrix} x_2 \\ -\frac{k_r}{m_p}x_1 + \frac{r_w K_w}{J_w}x_3 + \frac{r_w C_w}{J_w}x_4 - \frac{1}{2m_p} \rho_w C_d A_p (x_2 + rx_4 + x_6) |x_2 + rx_4 + x_6| + \frac{F_g - F_b}{m_p} \\ x_4 \\ -\frac{K_w}{J_w}x_3 - \frac{C_w}{J_w}x_4 \\ x_6 \\ 0 \end{bmatrix}$$

$$\mathbf{g} = \begin{bmatrix} 0 & -\frac{rT_w}{J_w} & 0 & \frac{T_w}{J_w} & 0 & 0 \end{bmatrix}^T$$

$$u = u_w$$

$$\mathbf{p} = [0 \quad -1 \quad 0 \quad 0 \quad 0 \quad 1]^T$$

where the motion of the vessel is considered as a disturbance $d = \ddot{Z}_{heave} + \ddot{\varphi}y_{tip}^b$. The output function is defined as $h(\mathbf{x}) = -x_1 + rx_3$, which is composed of the sum of the states $x_1(=\delta)$ and $x_3(=\theta)$. To achieve the predefined control objective, the output $h(\mathbf{x})$ should track the reference signal regardless of the disturbances. Therefore, using disturbance decoupling, we can derive a decoupled disturbance from the output if the system's relative degree is greater than or equal to the disturbance's relative degree and the disturbance is measurable [23].

In the case of a noncanonical nonlinear systems such as Eq.(4-3), its relative degree is not explicitly known [45]. Therefore, to design a control system, it is necessary to determine the relative degree of the system. The relative degree r_s of the system is defined in Eq.(4-4) [23].

$$\begin{aligned} L_g L_f^i h(\mathbf{x}) &= 0 \quad \forall i = 0, \dots, r_s - 2 \\ L_g L_f^{r_s-1} h(\mathbf{x}) &\neq 0 \end{aligned} \quad (4-4)$$

Also, the relative degree r_p of the disturbance is defined as follows

$$\begin{aligned}
L_p L_f^k h(\mathbf{x}) &= 0 \quad \forall k = 0, \dots, r_p - 2 \\
L_p L_f^{r_p - 1} h(\mathbf{x}) &\neq 0
\end{aligned} \tag{4-5}$$

where $L_a^i b(x)$ is a scalar function that represents the i th-order Lie derivative of $b(x)$ with respect to $a(x)$.

The relative degree of the output

The first-order derivative of the output with Lie derivative is given as

$$L_f^1 h(\mathbf{x}) + L_g^1 L_f^0 h(\mathbf{x})u = \frac{\partial h(\mathbf{x})}{\partial \mathbf{x}} [\mathbf{f}(\mathbf{x}) + \mathbf{g}u] = \dot{y} \tag{4-6}$$

where

$$L_g^1 L_f^0 h(\mathbf{x})u = L_g^1 h(\mathbf{x})u = \frac{\partial h(\mathbf{x})}{\partial \mathbf{x}} \mathbf{g} = 0$$

Since $L_g^1 h(\mathbf{x})u = 0$, the first-order derivative is $\dot{y} = L_f^1 h(\mathbf{x})$. Hence, \dot{y} is independent of control input u . The second-order derivative of the output is given by

$$L_r^2 h(\mathbf{x}) + L_g^1 L_r^1 h(\mathbf{x})u = \frac{\partial(L_r^1 h(\mathbf{x}))}{\partial \mathbf{x}} [\mathbf{f}(\mathbf{x}) + \mathbf{g}u] = \ddot{y} \quad (4-7)$$

where

$$L_r^1 h(\mathbf{x}) = \frac{\partial h(\mathbf{x})}{\partial \mathbf{x}} \mathbf{f}(\mathbf{x}) = -x_2 + rx_4$$

$$\begin{aligned} L_r^2 h(\mathbf{x}) &= \frac{\partial(L_r^1 h(\mathbf{x}))}{\partial \mathbf{x}} \mathbf{f}(\mathbf{x}) \\ &= -\mathbf{f}(2) + r\mathbf{f}(4) \\ &= \left(\frac{k_{eq}}{m_p} - \frac{k_{eq}}{J_w} \right) x_1 - \frac{2rC_w}{J_w} x_4 - \frac{2rK_w}{J_w} x_3 + \dots \\ &\quad \frac{1}{2m_p} \rho_w C_d A_p (x_2 + rx_4 + x_6) |x_2 + rx_4 + x_6| - \frac{1}{m_p} (F_g - F_b) \end{aligned}$$

$$\begin{aligned} L_g^1 L_r^1 h(\mathbf{x})u &= \frac{\partial(L_r^1 h(\mathbf{x}))}{\partial \mathbf{x}} \mathbf{g} \\ &= \left(\frac{rT_w}{J_w} + \frac{rT_w}{J_w} \right) u_w \neq 0 \end{aligned}$$

』

Since $L_g^1 L_r^1 h(\mathbf{x})u \neq 0$, we can conclude that the relative degree of the output is $r_s = 2$.

The relative degree of the disturbance

Similarly, the same procedure described in Eq.(4-6) and (4-7) is followed

to derive the relative degree of the disturbance. The resulting expression is as follows

$$L_p^1 L_f^1 h(\mathbf{x}) u = r \frac{T_w}{J_w} \neq 0 \quad (4-8)$$

where

$$L_f^1 h(\mathbf{x}) = \frac{\partial h(\mathbf{x})}{\partial \mathbf{x}} \mathbf{f}(\mathbf{x}) = -x_2 + rx_4$$

Hence, the relative degree of disturbance is $r_p = 2$. Therefore, the disturbance decoupling is possible. The control law based on the input-output linearization method, including the disturbance decoupling, is derived as follow[23],

$$u_w = \frac{-L_f^2 h(\mathbf{x}) - L_p^1 L_f^1 h(\mathbf{x}) d + v}{L_g^1 L_f^1 h(\mathbf{x})} \quad (4-9)$$

where v is the artificial input defined with the error state $\tilde{q} = r(\theta_d - \theta) + \delta$,

$$v = r\ddot{\theta}_d + k_1\dot{\tilde{q}} + k_2\tilde{q} \quad (4-10)$$

The linearization of the controller in Eq.(4-9) results in a simple linear relation $\ddot{y} = v$. Along with Eq.(4-10), we obtain

$$\ddot{\tilde{q}} + k_1\dot{\tilde{q}} + k_2\tilde{q} = 0 \quad (4-11)$$

where k_1 and k_2 are the state space feedback controller gains, which should be designed such that the roots of the polynomial Eq.(4-11) are strictly in the left-half plane. Then, the control law described in Eq.(4-9) yields a locally asymptotically stable compensator for the closed-loop system. To design these gains, the LQR (linear quadratic regulator) control technique is used with the controllable canonical form given as

$$\begin{bmatrix} \dot{\tilde{q}} \\ \ddot{\tilde{q}} \end{bmatrix} = \begin{bmatrix} 0 & 1 \\ 0 & 0 \end{bmatrix} \begin{bmatrix} \tilde{q} \\ \dot{\tilde{q}} \end{bmatrix} + \begin{bmatrix} 0 \\ 1 \end{bmatrix} u_q \quad (4-12)$$

$$u_q = - \begin{bmatrix} k_2 & k_1 \end{bmatrix} \begin{bmatrix} \tilde{q} \\ \dot{\tilde{q}} \end{bmatrix}$$

Defining the state as $\mathbf{z}_1 = [\tilde{q} \quad \dot{\tilde{q}}]^T$, the performance index is given as follows

$$J = \int_0^{\infty} (\mathbf{z}_1^T \mathbf{Q} \mathbf{z}_1 + R u_q^2) dt, \quad (4-13)$$

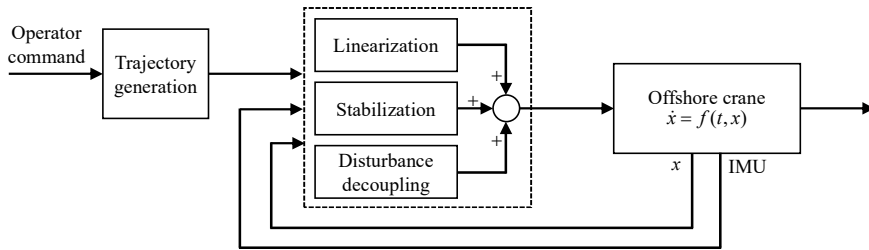


Figure 4-1. Control structure of the offshore crane with a input-output linearization

where $\mathbf{Q} = \text{diag}(q_1, q_2)$ is a positive definite matrix and R is a positive constant. Figure 4-1 shows a detailed illustration of the control structure.

4.3 Uniformly Ultimate Boundedness Control Design

As mentioned in the introduction, the classical feedback linearization technique is not robust if the nonlinearity is uncertain. Therefore, in this study, we introduce the control design method to cope with parametric variations based on uniformly ultimate boundedness (UUB) theory. The system model is redesigned, this time by integrating Eq.(4-3) with the input-output linearization controller. The energy-based Lyapunov function is then used to design the control law that should satisfy the UUB.

The control objective of this controller is tracking the desired position of the payload while regulating the wire rope variations. In other words, the state \tilde{q} and the rope variation δ should satisfy the following definition of UUB control theory

$$\begin{pmatrix} \|\tilde{q}(t_0)\| \\ \|\dot{\tilde{q}}(t_0)\| \\ \|\delta(t_0)\| \\ \|\dot{\delta}(t_0)\| \end{pmatrix} \leq a \Rightarrow \begin{pmatrix} \|\tilde{q}(t)\| \\ \|\dot{\tilde{q}}(t)\| \\ \|\delta(t)\| \\ \|\dot{\delta}(t)\| \end{pmatrix} \leq b, \quad \forall t \geq t_0 + T \quad (4-14)$$

To perform this control objective, an energy-based compensation control law is introduced. The proposed control law is defined by a summation of the input-output linearization controller u_{w1} and the energy-based compensation u_{w2} , that is

$$u_w = u_{w1} + u_{w2} \quad (4-15)$$

For the sake of notational simplicity, Eq.(4-9) is represented as follow

$$u_{w1} = \frac{-L_f^2 h(\mathbf{x}) - L_p^1 L_f h(\mathbf{x})d + v}{L_g^1 L_f h(\mathbf{x})} := \frac{-F_1 - D + v}{G_1} \quad (4-16)$$

Taking into consideration the total control law in Eq.(4-15), and substituting Eq.(4-16) into the second-order derivative of the output equation, the dynamic model without disturbance can be rewritten as follow

$$\frac{d}{dt} \begin{bmatrix} \tilde{q} \\ \dot{\tilde{q}} \\ \delta \\ \dot{\delta} \end{bmatrix} = \begin{bmatrix} \dot{\tilde{q}} \\ -k_1\dot{\tilde{q}} - k_2\tilde{q} - G_1u_{w2} \\ \dot{\delta} \\ F_2 + G_2u_{w1} + G_2u_{w2} \end{bmatrix} \quad (4-17)$$

where $G_1 = 2r_w T_w / J_w$, $G_2 = -r_w T_w / J_w$ and F_2 represents the remainder term except the control input term of Eq.(3-31).

In order to design the controller u_{w2} , we propose the following energy-based Lyapunov function such as

$$V = \frac{\sigma}{2} \mathbf{z}_1^T \mathbf{A}_{11} \mathbf{z}_1 + \frac{1}{2} \mathbf{z}_2^T \mathbf{A}_{22} \mathbf{z}_2 + \gamma(\delta) \quad (4-18)$$

where $\mathbf{z}_1 = [\tilde{q} \ \dot{\tilde{q}}]^T$, $\mathbf{z}_2 = [\delta \ \dot{\delta}]^T$ and \mathbf{A}_{11} , \mathbf{A}_{22} are symmetric matrices such as

$$\mathbf{A}_{11} = \begin{bmatrix} k_2 & c_1 \\ c_1 & 1 \end{bmatrix}, \mathbf{A}_{22} = \begin{bmatrix} k_3 & c_2 \\ c_2 & 1 \end{bmatrix} \quad (4-19)$$

where σ , c_1 , c_2 , k_3 are positive constants. $\gamma(\delta)$ is a function to be defined according to the requirements to guarantee the uniform boundedness of the trajectories. In order to ensure that Eq.(4-18) is positive definite,

$\gamma(\delta)$, the design function must satisfy the following conditions

$$\frac{1}{2}k_3\delta^2 + \gamma(\delta) \geq \frac{\alpha}{2}\delta^2, \quad \gamma(0) = 0 \quad (4-20)$$

For all $|\delta| < r$, with a α being a positive constant. Under these conditions, the function V satisfies the lower bound criterion

$$V \geq \frac{\sigma}{2} \begin{bmatrix} \tilde{q} \\ \dot{\tilde{q}} \end{bmatrix}^T \begin{bmatrix} k_2 & c_1 \\ c_1 & 1 \end{bmatrix} \begin{bmatrix} \tilde{q} \\ \dot{\tilde{q}} \end{bmatrix} + \frac{1}{2} \begin{bmatrix} \delta \\ \dot{\delta} \end{bmatrix}^T \begin{bmatrix} \alpha & c_2 \\ c_2 & 1 \end{bmatrix} \begin{bmatrix} \delta \\ \dot{\delta} \end{bmatrix} \quad (4-21)$$

with the restrictions on $c_1 < \sqrt{k_2}$ and $c_2 < \sqrt{\alpha}$, the function V is now positive definite and radially unbounded. The time derivative of V along the trajectories of the closed-loop system in Eq.(4-17) is as follows

$$\begin{aligned} \dot{V} = & -\sigma \begin{bmatrix} \tilde{q} \\ \dot{\tilde{q}} \end{bmatrix}^T \begin{bmatrix} c_1 k_2 & \frac{1}{2} c_1 k_1 \\ \frac{1}{2} c_1 k_1 & k_1 - c_1 \end{bmatrix} \begin{bmatrix} \tilde{q} \\ \dot{\tilde{q}} \end{bmatrix} \\ & + (c_2 G_2 \delta + G_2 \dot{\delta} - \sigma G_1 c_1 \tilde{q} - \sigma G_1 \dot{\tilde{q}}) u_{w2} \\ & + k_3 \delta \dot{\delta} + c_2 \dot{\delta}^2 + (F_2 + G_2 u_{w1})(\dot{\delta} + c_2 \delta) + \dot{\gamma}(\delta) \dot{\delta} \end{aligned} \quad (4-22)$$

We noted that Eq.(4-22) is not expressed in quadratic form by state δ

and $\dot{\delta}$. Hence, it is necessary to introduce some quadratic terms for state δ into the time derivative of V to guarantee the uniformly ultimately bounded of the nonlinear system Eq.(4-17). Thus, we propose the energy-based compensation control law u_{w2} given as

$$u_{w2} = -\varepsilon(c_2 G_2 \delta + G_2 \dot{\delta} - \sigma c_1 G_1 \tilde{q} - \sigma G_1 \dot{\tilde{q}}) - k_3 G_2 \delta - k_4 G_2 \dot{\delta} \quad (4-23)$$

where ε and k_4 are positive constants. Substituting the Eq.(4-23) into (4-22), the time derivative of V is obtained as follow

$$\begin{aligned} \dot{V} = & -\sigma \begin{bmatrix} \tilde{q} \\ \dot{\tilde{q}} \end{bmatrix}^T \begin{bmatrix} c_1 k_2 & \frac{1}{2} c_1 k_1 \\ \frac{1}{2} c_1 k_1 & k_1 - c_1 \end{bmatrix} \begin{bmatrix} \tilde{q} \\ \dot{\tilde{q}} \end{bmatrix} \\ & - \varepsilon (c_2 G_2 \delta + G_2 \dot{\delta} - \sigma G_1 c_1 \tilde{q} - \sigma G_1 \dot{\tilde{q}})^2 \\ & - (c_2 G_2 \delta + G_2 \dot{\delta} - \sigma G_1 c_1 \tilde{q} - \sigma G_1 \dot{\tilde{q}}) k_3 G_2^2 \delta \\ & - (c_2 G_2 \delta + G_2 \dot{\delta} - \sigma G_1 c_1 \tilde{q} - \sigma G_1 \dot{\tilde{q}}) k_4 G_2 \dot{\delta} \\ & + c_2 \dot{\delta}^2 + k_3 \delta \dot{\delta} + (F_2 + G_2 u_{w1}) (\dot{\delta} + c_2 \delta) + \dot{\gamma}(\delta) \dot{\delta} \end{aligned} \quad (4-24)$$

then, Eq.(4-24) can be rewritten by joining common terms as follow

$$\begin{aligned}
\dot{V} = & -\sigma \begin{bmatrix} \tilde{q} \\ \dot{\tilde{q}} \end{bmatrix}^T \begin{bmatrix} c_1 k_2 & \frac{1}{2} c_1 k_1 \\ \frac{1}{2} c_1 k_1 & k_1 - c_1 \end{bmatrix} \begin{bmatrix} \tilde{q} \\ \dot{\tilde{q}} \end{bmatrix} \\
& - \varepsilon (c_2 G_2 \delta + G_2 \dot{\delta} - \sigma G_1 c_1 \tilde{q} - \sigma G_1 \dot{\tilde{q}})^2 \\
& + \begin{bmatrix} \delta \\ \dot{\delta} \end{bmatrix}^T \begin{bmatrix} \sigma k_3 c_1 G_1 G_2 & \sigma k_3 G_1 G_2 \\ \sigma c_1 k_4 G_1 G_2 & \sigma k_4 G_1 G_2 \end{bmatrix} \begin{bmatrix} \tilde{q} \\ \dot{\tilde{q}} \end{bmatrix} \\
& - \begin{bmatrix} \delta \\ \dot{\delta} \end{bmatrix}^T \begin{bmatrix} c_2 k_3 G_2^2 & \frac{1}{2} c_2 k_4 G_2^2 \\ \frac{1}{2} c_2 k_4 G_2^2 & k_4 G_2^2 - c_2 \end{bmatrix} \begin{bmatrix} \delta \\ \dot{\delta} \end{bmatrix} \\
& - k_3 G_2^2 \delta \dot{\delta} + k_3 \delta \dot{\delta} + (F_2 + G_2 u_{w1}) (\dot{\delta} + c_2 \delta) + \dot{\gamma}(\delta) \delta
\end{aligned} \tag{4-25}$$

As a results, the first to fourth lines of Eq.(4-25) can be expressed in quadratic form. However, undesired cross terms depending on $\delta \dot{\delta}$ are introduced by control input u_{w2} . In order to eliminate such cross terms, we propose the function $\dot{\gamma}(\delta)$ as follow

$$\dot{\gamma}(\delta) = (k_3 G_2^2 \delta - k_3 \delta) \tag{4-26}$$

by integrating Eq.(4-26), we can easily compute the explicit function $\gamma(\delta)$ as follow

$$\begin{aligned}
\gamma(\delta) &= \int (k_3 G_2^2 \delta - k_3 \delta) d\delta \\
&= -\frac{1}{2} k_3 \delta^2 + \frac{1}{2} k_3 G_2^2 \delta^2
\end{aligned} \tag{4-27}$$

The function in Eq.(4-27) should satisfy the conditions of Eq.(4-20). From Eq.(4-20) and Eq.(4-27), the resulting inequality is as follows

$$\alpha \leq k_3 G_2^2, \quad c_2 < |G_2| \sqrt{k_3} \tag{4-28}$$

therefore, the positive definiteness of V is guaranteed by inequality Eq.(4-28).

By substituting the function $\gamma(\delta)$ into Eq.(4-25), the expression of time derivative of V can be rewritten as follow

$$\begin{aligned}
\dot{V} = & -\sigma \begin{bmatrix} \tilde{q} \\ \dot{\tilde{q}} \end{bmatrix}^T \begin{bmatrix} c_1 k_2 & \frac{1}{2} c_1 k_1 \\ \frac{1}{2} c_1 k_1 & k_1 - c_1 \end{bmatrix} \begin{bmatrix} \tilde{q} \\ \dot{\tilde{q}} \end{bmatrix} \\
& - \varepsilon (c_2 G_2 \delta + G_2 \dot{\delta} - \sigma G_1 c_1 \tilde{q} - \sigma G_1 \dot{\tilde{q}})^2 \\
& + \begin{bmatrix} \delta \\ \dot{\delta} \end{bmatrix}^T \begin{bmatrix} \sigma k_3 c_1 G_1 G_2 & \sigma k_3 G_1 G_2 \\ \sigma c_1 k_4 G_1 G_2 & \sigma k_4 G_1 G_2 \end{bmatrix} \begin{bmatrix} \tilde{q} \\ \dot{\tilde{q}} \end{bmatrix} \\
& - \begin{bmatrix} \delta \\ \dot{\delta} \end{bmatrix}^T \begin{bmatrix} c_2 k_3 G_2^2 & \frac{1}{2} c_2 k_4 G_2^2 \\ \frac{1}{2} c_2 k_4 G_2^2 & k_4 G_2^2 - c_2 \end{bmatrix} \begin{bmatrix} \delta \\ \dot{\delta} \end{bmatrix} \\
& + (F_2 + G_2 u_{w1}) (\dot{\delta} + c_2 \delta)
\end{aligned} \tag{4-29}$$

We note from Eq.(4-29) that undesired cross terms are eliminated, and then \dot{V} is written in a quadratic form through proper definition of the u_{w2} and $\gamma(\delta)$. The next step is to show the uniformly ultimately boundedness of the state \tilde{q} and the rope variation δ with the proposed controller Eq.(4-15). Figure 4-2 shows a detailed illustration of the control structure.

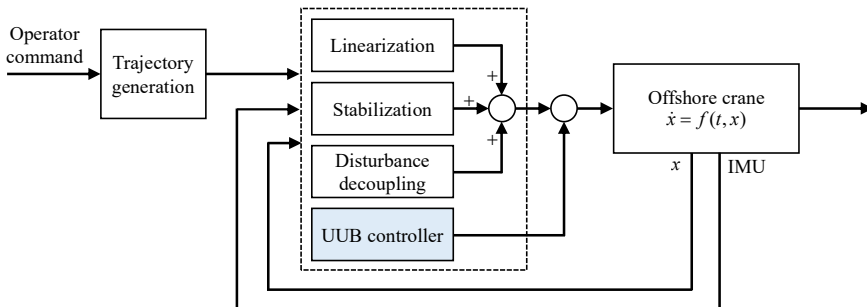


Figure 4-2. Control structure of the offshore crane with UUB controller

Closed Loop System Analysis

Along with Eq.(4-29), the expression of \dot{V} can be rewritten in matrix form as follow

$$\dot{V} = - \begin{bmatrix} \tilde{q} \\ \dot{\tilde{q}} \\ \delta \\ \dot{\delta} \end{bmatrix}^T \begin{bmatrix} \mathbf{A} & \mathbf{B} \\ \mathbf{B}^T & \mathbf{C} \end{bmatrix} \begin{bmatrix} \tilde{q} \\ \dot{\tilde{q}} \\ \delta \\ \dot{\delta} \end{bmatrix} - \varepsilon U^2 + \Delta \quad (4-30)$$

where

$$\mathbf{A} = \begin{bmatrix} c_1 k_2 & \frac{1}{2} c_1 k_1 \\ \frac{1}{2} c_1 k_1 & k_1 - c_1 \end{bmatrix}, \mathbf{B} = -\frac{1}{2} \begin{bmatrix} \sigma k_3 c_1 G_1 G_2 & \sigma k_3 G_1 G_2 \\ \sigma c_1 k_4 G_1 G_2 & \sigma k_4 G_1 G_2 \end{bmatrix},$$

$$\mathbf{C} = \begin{bmatrix} c_2 k_3 G_2^2 & \frac{1}{2} c_2 k_4 G_2^2 \\ \frac{1}{2} c_2 k_4 G_2^2 & k_4 G_2^2 - c_2 \end{bmatrix},$$

$$\begin{aligned} U &= (c_2 G_2 \delta + G_2 \dot{\delta} - \sigma G_1 c_1 \tilde{q} - \sigma G_1 \dot{\tilde{q}}) \\ &= [-\sigma G_1 c_1 \quad -\sigma G_1 \quad c_2 G_2 \quad G_2] \mathbf{z} \\ &= \mathbf{U}_c \mathbf{z}, \end{aligned}$$

$$\Delta = (F_2 + G_2 u_{w1})(\dot{\delta} + c_2 \delta)$$

Defining the state $\mathbf{z} = [\tilde{q} \quad \dot{\tilde{q}} \quad \delta \quad \dot{\delta}]^T$, then the U^2 can be rewritten as

$$U^2 = \mathbf{z}^T \mathbf{U}_c^T \mathbf{U}_c \mathbf{z} = \mathbf{z}^T \mathbf{D} \mathbf{z} \quad (4-31)$$

Along with aforementioned matrix expression of \dot{V} , we can determine the upper bound of \dot{V} as follows

$$\begin{aligned} \dot{V} &\leq -\lambda_{\min}(\mathbf{A}) \|\mathbf{z}_1\|^2 + 2\|\mathbf{B}\| \|\mathbf{z}_1\| \|\mathbf{z}_2\| - \lambda_{\min}(\mathbf{C}) \|\mathbf{z}_2\|^2 - \varepsilon \lambda_{\min}(\mathbf{D}) \|\mathbf{z}\|^2 + \Delta_{\max} \\ &\leq -\lambda_{\min}(\mathbf{H}) \|\mathbf{z}\|^2 - \varepsilon \lambda_{\min}(\mathbf{D}) \|\mathbf{z}\|^2 + \Delta_{\max} \\ &= -(\lambda_{\min}(\mathbf{H}) + \varepsilon \lambda_{\min}(\mathbf{D})) \|\mathbf{z}\|^2 + \Delta_{\max} \end{aligned} \quad (4-32)$$

where the $\lambda(\cdot)$ represents the eigenvalues of a matrix and

$$\mathbf{H} = \begin{bmatrix} \lambda_{\min}(\mathbf{A}) & -\|\mathbf{B}\| \\ -\|\mathbf{B}\| & \lambda_{\min}(\mathbf{C}) \end{bmatrix} \quad (4-33)$$

with Δ_{\max} is a positive constant satisfying $\Delta \leq \Delta_{\max}$. By assuming the existence of the conditions that ensure $\lambda_{\min}(\mathbf{H}) + \varepsilon \lambda_{\min}(\mathbf{D}) > 0$, it is possible to establish the upper bound of \dot{V} as

$$\dot{V} \leq -(\lambda_{\min}(\mathbf{H}) + \varepsilon\lambda_{\min}(\mathbf{D}) - \kappa)\|\mathbf{z}\|^2 + \Delta_{\max} - \kappa\|\mathbf{z}\|^2 \quad (4-34)$$

where $0 < \kappa < \lambda_{\min}(\mathbf{H}) + \varepsilon\lambda_{\min}(\mathbf{D})$. Then,

$$\dot{V} \leq -(\lambda_{\min}(\mathbf{H}) + \varepsilon\lambda_{\min}(\mathbf{D}) - \kappa)\|\mathbf{z}\|^2, \quad \forall \|\mathbf{z}\| \geq \sqrt{\frac{\Delta_{\max}}{\kappa}} := \Omega \quad (4-35)$$

which proves that the inequality conditions of the uniformly ultimate boundedness are satisfied. Additionally, the ultimate bound of the state $\|\mathbf{z}\| \leq b$, $\forall t \geq t_0 + T$ can be derived using the functions α_1 and α_2 .

$$\alpha_1(\|\mathbf{z}\|) \leq V \leq \alpha_2(\|\mathbf{z}\|) \quad (4-36)$$

After carefully analyzing the upper and lower bounds of V , we can derive their final expressions as follows

$$\begin{aligned} V &\geq \frac{1}{2} \mathbf{z}^T \mathbf{A}^* \mathbf{z} \geq \frac{1}{2} \lambda_{\min}(\mathbf{A}^*) \|\mathbf{z}\|^2 \\ V &\leq \frac{1}{2} \mathbf{z}^T \mathbf{A} \mathbf{z} + \gamma(\delta) \leq \frac{1}{2} \lambda_{\max}(\mathbf{A}) \|\mathbf{z}\|^2 + |\mu| \|\mathbf{z}\|^2 \end{aligned} \quad (4-37)$$

where

$$\mathbf{A}^* = \begin{bmatrix} \sigma \mathbf{A}_{11} & \mathbf{0}_{2 \times 2} \\ \mathbf{0}_{2 \times 2} & \mathbf{A}_{22}^* \end{bmatrix}, \mathbf{A} = \begin{bmatrix} \sigma \mathbf{A}_{11} & \mathbf{0}_{2 \times 2} \\ \mathbf{0}_{2 \times 2} & \mathbf{A}_{22} \end{bmatrix} \quad (4-38)$$

$$\mu = \frac{1}{2} k_3 (G_2^2 - 1) \quad (4-39)$$

According to Eq.(4-36), Eq.(4-37) can be rewritten as

$$\begin{aligned} \alpha_1(r) &= \frac{1}{2} \lambda_{\min}(\mathbf{A}^*) r^2 \\ \alpha_2(r) &= \frac{1}{2} \lambda_{\max}(\mathbf{A}) r^2 + |\mu| r^2 \end{aligned} \quad (4-40)$$

Thus, the ultimate bound b is calculated as follows

$$b = \alpha_1^{-1}(\alpha_2(\Omega)) = \sqrt{\frac{\lambda_{\max}(\mathbf{A}) \Omega^2 + 2|\mu| \Omega^2}{\lambda_{\min}(\mathbf{A}^*)}} \quad (4-41)$$

4.4 Integral Sliding Mode Controller Design

Consider a couple of sliding surfaces augmented by an integral action with a nonzero initial state term as the following

$$S = s_1 + s_2 \quad (4-42)$$

where

$$\begin{aligned} s_1 &= g_1 \dot{e}_\theta + g_2 e_\theta + \int_0^t g_3 e_\theta(\tau) d\tau - s_1(0) \\ s_2 &= \int_0^t g_4 \delta(\tau) d\tau + g_5 \delta - s_2(0) \end{aligned} \quad (4-43)$$

g_1, \dots, g_5 are real positive constants and $e_\theta = \theta_d - \theta$, where θ_d is the desired value of θ . The sliding surface in Eq.(4-42) always satisfies $S(t) = 0$ at $t = 0$ based on the initial states of $s_1(0)$ and $s_2(0)$. Therefore, from the start the controlled system can slide along the surface without a reaching phase. To design the control law, the conventional Lyapunov function $V = (1/2)S^2$ is employed. Then the time derivatives of the V is calculated as follows

$$\begin{aligned} \dot{V} &= S\dot{S} \\ &= S(g_1 \ddot{e}_\theta + g_2 \dot{e}_\theta + g_3 e_\theta + g_4 \dot{\delta} + g_5 \delta) \end{aligned} \quad (4-44)$$

Based on Eq.(4-44), the control input which yields $\dot{V} \leq 0$ is derived as the following

$$u_w = \frac{C_w}{T_w} \dot{\theta} + \frac{K_w}{T_w} \theta - \frac{J_w}{T_w g_1} (g_2 \dot{e}_\theta + g_3 e_\theta + g_4 \dot{\delta} + g_5 \delta + K \text{sgn}(S)) \quad (4-45)$$

where, $K \geq g_1 |\max(\ddot{\theta}_d)| + \eta$, and η is a strictly positive constant. The second derivative of the V is derived in Eq.(4-46), then the uniform continuity of \dot{V} can be shown easily.

$$\ddot{V} = -K \frac{S}{|S|} \dot{S} = -\frac{1}{|S|} K S \dot{S} = -\frac{1}{|S|} K (-K |S|) = K^2 \quad (4-46)$$

Therefore, based on Barbalat's lemma, we can show that $\dot{V} \rightarrow 0$ as $t \rightarrow \infty$. In other words, V approaches a finite value, such that $V_{t \rightarrow \infty} \leq V(S(0), 0)$. As a result, the sliding surface S converges to zero.

However, the convergence of the state e_θ and δ cannot be achieved simultaneously since the sliding surface in Eq.(4-42) is coupled. Furthermore, with the presence of parametric variations, especially parameters of the submerged system (the added mass of the payload and the hydrodynamic coefficient), undesired perturbed motions can appear in the state e_θ and δ . To overcome this problem, authors in [46]–[48] proposed a robust stability analysis method for nonlinear systems.

In this section, and based on this method, the robust stability of the

offshore crane system is conducted. Assuming that the system remains on the sliding surface $S = 0$ and $\dot{S} = 0$, with the state $\mathbf{v} = [e_\theta \quad \dot{e}_\theta \quad \delta \quad \dot{\delta}]^T$, then the closed-loop system is described as

$$\dot{\mathbf{v}} = \mathbf{f}(\mathbf{v}) \quad (4-47)$$

where

$$\mathbf{f}(\mathbf{v}) = \begin{bmatrix} v_2 \\ -g_1^{-1}(g_3v_1 + g_2v_2 + g_4v_3 + g_5v_4) - \ddot{\theta}_d \\ \zeta_4 \\ -k_r m_p^{-1} v_3 - g_1^{-1}(g_3v_1 + g_2v_2 + g_4v_3 + g_5v_4) - F^* \end{bmatrix}$$

where $F^* = -\ddot{Z}_{heave} - \ddot{\varphi} y_{ip}^b + (F_g - F_b) / m_p + f_h / m_p$. Considering the behavior around the equilibrium points, we can assume that the k_r is constant. Then the linearized model of the nonlinear system Eq.(4-47) can be obtained as

$$\dot{\mathbf{v}} = \mathbf{A}\mathbf{v} \quad (4-48)$$

$$\begin{bmatrix} \dot{v}_1 \\ \dot{v}_2 \\ \dot{v}_3 \\ \dot{v}_4 \end{bmatrix} = \begin{bmatrix} 0 & 1 & 0 & 0 \\ -g_3/g_1 & -g_2/g_1 & -g_4/g_1 & -g_5/g_1 \\ 0 & 0 & 0 & 1 \\ -g_3/g_1 & -g_2/g_1 & -g_4/g_1 - k_r/m_p & -g_5/g_1 \end{bmatrix} \begin{bmatrix} v_1 \\ v_2 \\ v_3 \\ v_4 \end{bmatrix}$$

According to Lyapunov's linearization method [49], if the linearized system is strictly stable, the equilibrium point is asymptotically stable. Therefore, we can focus on finding a sufficient condition that the characteristic equation of the linear system in Eq.(4-48) satisfies the Hurwitz stability criterion. As a result, we can obtain the following inequality conditions

$$\begin{aligned} g_1, g_2, g_3, g_4, g_5 &> 0 \\ g_2 g_4 &> g_3 g_5 \end{aligned} \quad (4-49)$$

As a result, the closed-loop system with the control law described in Eq.(4-45) and the condition Eq.(4-49), all the controlled variables asymptotically converge to their desired values regardless of the parametric variations.

4.5 Controller Gain Optimization

In this section, the optimization method of the designed controller gain is introduced. Generally, a trial and error process that helps to select the

controller gains is performed. However, it does not guarantee an optimal value that guarantees the best performance. Therefore, a modern optimization algorithm is required to define optimal gains in an auto-manner. Hence, in this study, the PSO technique is applied to reach the optimal controller gains.

To evaluate the cost of each particle, the performance index (objective function) is used. Integral of absolute error (IAE), the integral of squared error (ISE), or integral of time-weighted-squared-error (ITSE) are examples of these indices. After careful analysis of the advantages and disadvantages of performance indices, the adopted optimization problem is described as follows

$$\min J = \int_0^{\infty} |e_p(t)| \quad (4-50)$$

where $e_p = P_{ref}^n - p_{load,z}^n$. However, it is necessary to satisfy the stability conditions of the closed-loop system as well as the optimization problem. In other words, the selected controller gains need to satisfy the stability conditions. Therefore, the optimization problem can be rewritten by the addition of a penalty term ($\mathbf{I}^T \boldsymbol{\Sigma} \mathbf{I}$) as such

$$\min J = \int_0^{\infty} |e_p(t)| + \mathbf{I}^T \boldsymbol{\Sigma} \mathbf{I} \quad (4-51)$$

where $\mathbf{I}_{n \times 1} = [1 \ \cdots \ 1]^T$ and $\mathbf{\Sigma} = \text{diag}(\varsigma_1, \dots, \varsigma_n)$. In the matrix $\mathbf{\Sigma}$, the stability conditions are satisfied. For the input-output linearization controller, the diagonal terms are as follows

$$\varsigma_1 = \begin{cases} 0, & \text{if } q_1, q_2, R > 0 \\ \infty, & \text{else} \end{cases}, \quad (4-52)$$

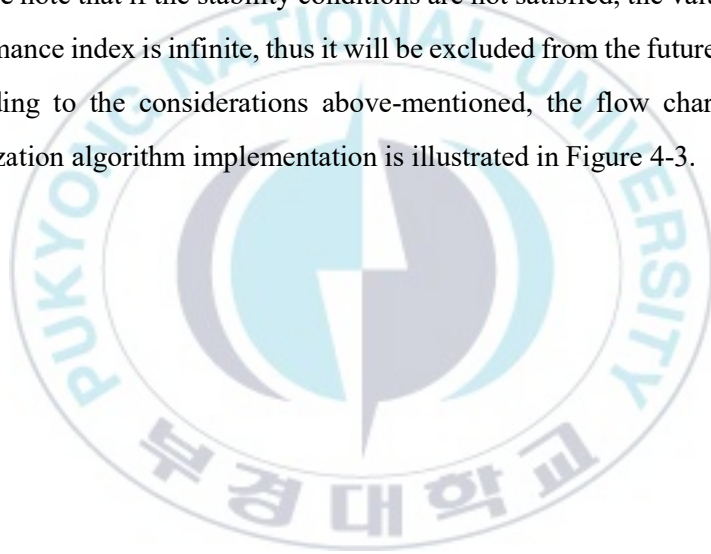
for the UUB controller,

$$\begin{aligned} \varsigma_1 &= \begin{cases} 0, & \text{if } \sigma, k_3, k_4, c_1, c_2, \varepsilon > 0 \\ \infty, & \text{else} \end{cases} \\ \varsigma_2 &= \begin{cases} 0, & \text{if } \sqrt{k_2} > c_1 \\ \infty, & \text{else} \end{cases} \\ \varsigma_3 &= \begin{cases} 0, & \text{if } |G| \sqrt{k_3} > c_2 \\ \infty, & \text{else} \end{cases} \\ \varsigma_4 &= \begin{cases} 0, & \text{if } \lambda_{\min}(\mathbf{H}) + \varepsilon \lambda_{\min}(\mathbf{D}) > 0 \\ \infty, & \text{else} \end{cases} \end{aligned} \quad (4-53)$$

And finally, in the case of the integral sliding mode controller, the diagonal terms are calculated as the following

$$\begin{aligned}
\varsigma_1 &= \begin{cases} 0, & \text{if } g_1, g_2, g_3, g_4, g_5 > 0 \\ \infty, & \text{else} \end{cases} \\
\varsigma_2 &= \begin{cases} 0, & \text{if } g_2 g_4 > g_3 g_5 \\ \infty, & \text{else} \end{cases} \\
\varsigma_3 &= \begin{cases} 0, & \text{if } K \geq g_1 |\max(\ddot{\theta}_d)| + \eta \\ \infty, & \text{else} \end{cases}
\end{aligned} \tag{4-54}$$

We note that if the stability conditions are not satisfied, the value of the performance index is infinite, thus it will be excluded from the future swarm. According to the considerations above-mentioned, the flow chart of the optimization algorithm implementation is illustrated in Figure 4-3.



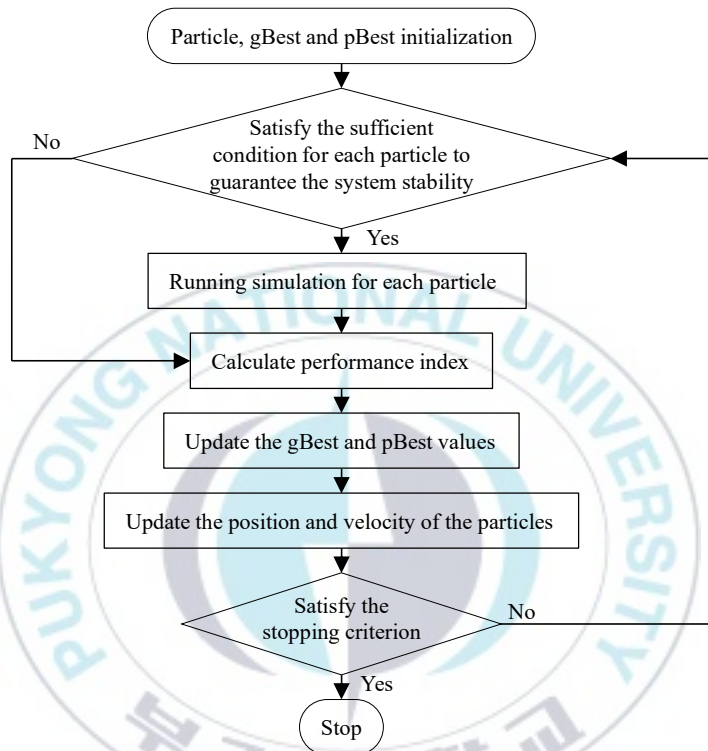


Figure 4-3. Controller gain optimization flow chart using PSO

5 Simulation with Virtual Offshore Crane

5.1 Simulation Setup

To show the usefulness of the offshore crane control system with simulation tests, the dynamic model derived in chapter 3 is used. The ship motions are generated by a wave obtained from Marine System Simulator toolbox (MSS) supported by MATLAB/Simulink, which was developed by researchers affiliated to Thor I. Fossen's team.

The type of ship used is a supply vessel, and the wave is generated with the JONSWAP spectrum [32]. All the detailed specifications are listed in Table 5-1, which were selected after careful analysis of the vessel's response. Figure 5-1 represents the definition of wave encounter angle. The vessel motion is analyzed with motion RAO (Response Amplitude Operator) in the MSS toolbox.

Table 5-1 Parameters of vessel and wave used in simulation

Item	Description	Value
Vessel	Draft (m)	6
	Breadth (m)	19.2
	Length between perpendiculars (m)	82.8
	Mass (ton)	6,362
Wave	Encounter angle (deg)	90
	Peak frequency (rad/s)	0.6
	Height amplitude (m)	3

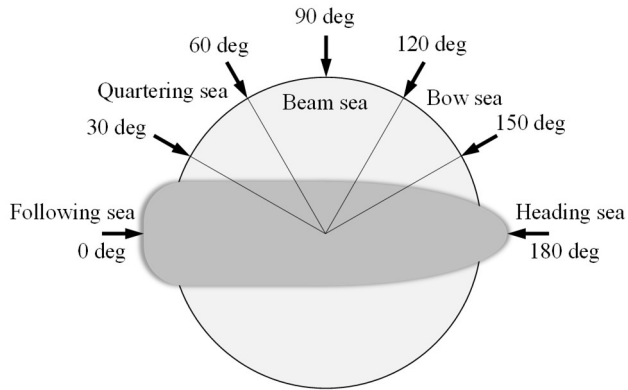


Figure 5-1. Definition of wave encounter's angle

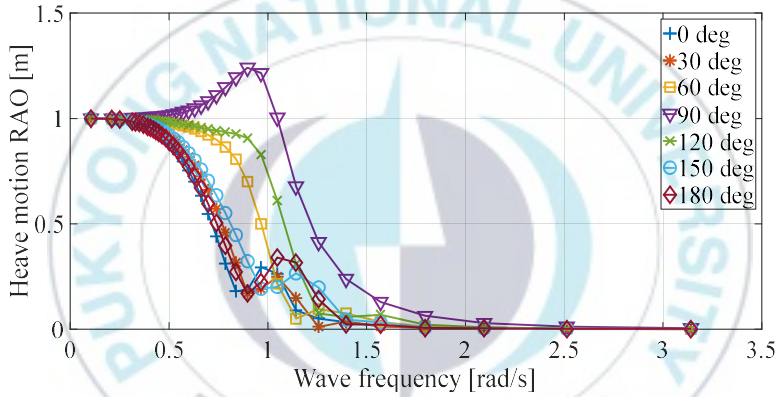


Figure 5-2. Heave motion RAO of vessel

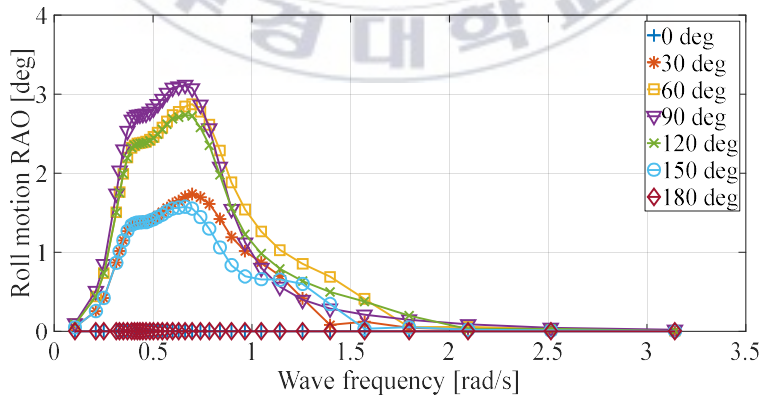


Figure 5-3. Roll motion RAO of vessel

Figure 5-2 and Figure 5-3 represent the results of motion RAO with the vessel and the wave above-mentioned. As shown in the result of motion RAO, the roll motion and heave motion are greatest when the wave encounter angle is 90deg with a velocity of 0.6~0.9rad/s. Hence, the 90deg and 0.6rad are selected to be used in the simulation.

The desired position of the payload p_{ref}^n is set to alternate a 2[m] descending motion for 15 seconds and a 2[m] ascending motion after 45 seconds with $|\ddot{\theta}_d|_{\max} = 0.9 \text{ rad/s}^2$. In order to guarantee that the movement of the payload is sufficiently smooth, a third-order Hermite interpolation is used by using MATLAB. The resulting desired position of the payload is illustrated in Figure 5-4.

The offshore crane system nominal parameters used in the simulation are listed in Table 5-2. The wave disturbance, given as $y_{tip}^b \varphi + Z_{heave}$ is represented in Figure 5-5.

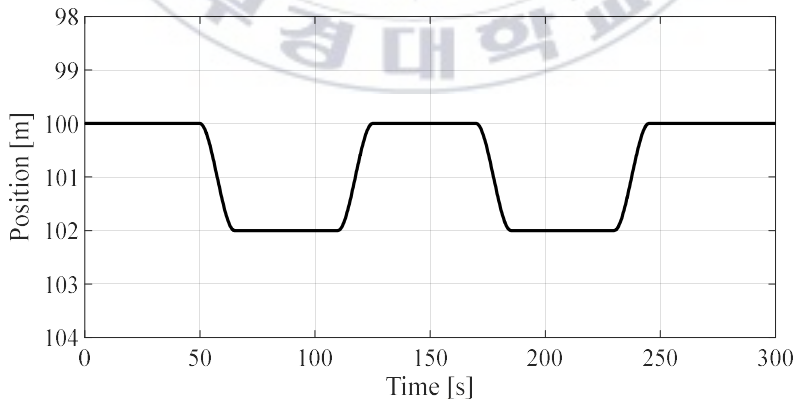


Figure 5-4. Desired position of the payload

Table 5-2. Parameter of offshore crane system used in simulation

Parameter	Value	Parameter	Value		
m	Mass of payload(kg)	43,200	ρ_w	Density of water(kg/m ³)	1,000
C_p	Added mass coefficient of payload(-)	1.5	y_{tip}^b	y directional crane tip position in b-frame(m)	5
V_p	Volume of payload(m ³)	4	J_w	Inertia moment(kg.m ²)	15,700
EA_r	Elasticity modulus × cross section of cable(N)	4.55×10^7	C_w	Damping coefficient(Pa.s)	7,000
C_D	Drag coefficient(-)	1	K_w	Spring coefficient(N/m)	2,000
A_p	Cross-section in the vertical direction of payload(m ²)	5	T_w	Torque constant(-)	2,500
$l_w(0)$	Initial length of rope(m)	100	r_w	Radius of winch drum(m)	1

The controller's gain optimization step is conducted by using MATLAB/Simulink. The optimization and simulation results are listed in Table 5-3. Where IOLC is the input-output linearization controller, UUB-

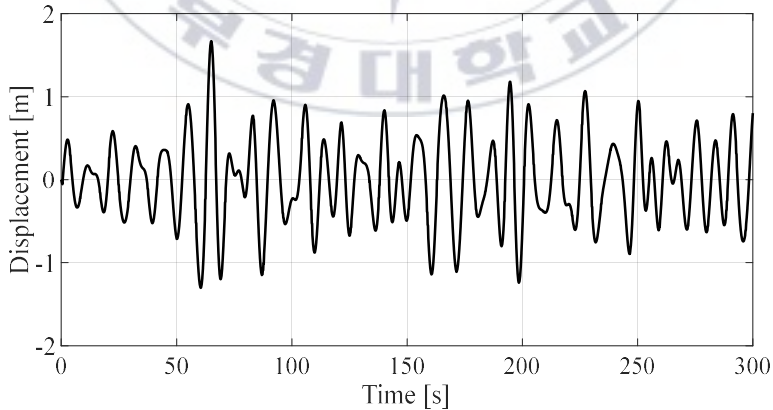


Figure 5-5. Wave disturbance displacement

Table 5-3. Optimized controller gain and the results of performance index

Controller	Gain	$J = \int_0^{\infty} e_p(t) $
IOLC	$q_1 = 23.6403, q_2 = 635.4978, R = 1.3705$ $\rightarrow k_1 = 21.7257, k_2 = 4.1532$ $k_1 = 21.7257, k_2 = 4.1532$	11.4412
UUB-IOLC	$\sigma = 2.2649 \times 10^{-4}, k_3 = 83.0236, k_4 = 12.6669,$ $c_1 = 0.0397, c_2 = 0.3088, \varepsilon = 18.6023$	5.2364
ISMC	$g_1 = 45.7788, g_2 = 35.5351, g_3 = 0.0926,$ $g_4 = 0.0541, g_5 = 6.8193, \eta = 0.9356 (K = 42.1366)$	3.2119

IOLC is the UUB based controller integrated with IOLC, ISMC is the integral sliding mode controller.

As depicted in the results, the performance index J in the case of ISMC is the smallest and IOLC is the largest. In the next section, we evaluate the simulation results with the nominal model and uncertain model.

5.2 Simulation Results

5.2.1 Simulation with Nominal Model

Simulation results with the nominal model are presented in Figure 5-6~Figure 5-11. Figure 5-6 represents the payload position response without compensation controller. In this case, a simple feedforward controller is applied to track the resulting desired position of payload. Therefore, the

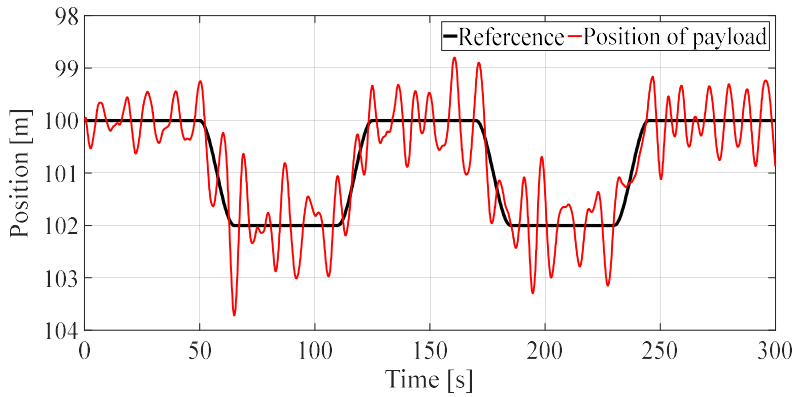


Figure 5-6. Payload position response without compensation controller

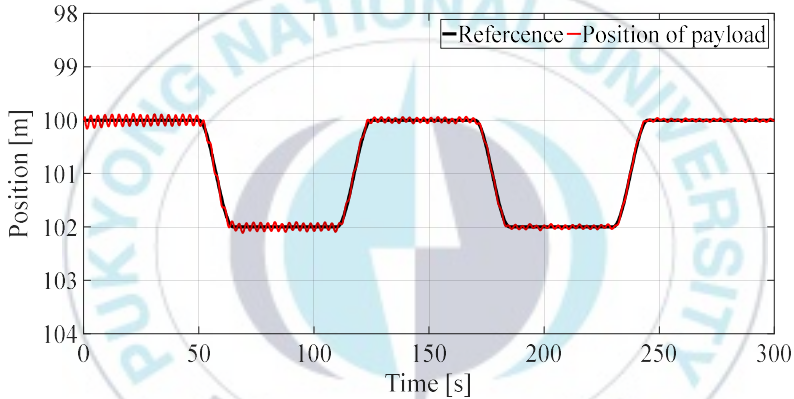


Figure 5-7. Payload position response with IOLC

impact of disturbances is not suppressed in the payload's positioning response as well as the rope tension response shown in Figure 5-11. Figure 5-6~Figure 5-8 represent, respectively, the payload position response of the IOLC, UUB+IOLC, ISMC control systems.

It is clear that the payload's position follows the desired signal well. However, as shown in Figure 5-7, residual vibrations continuously appear in the payload position as well as the rope tension responses.

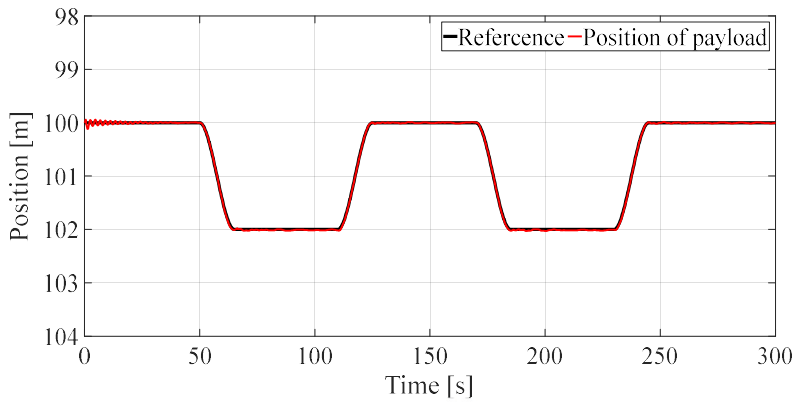


Figure 5-8. Payload position response with ISMC

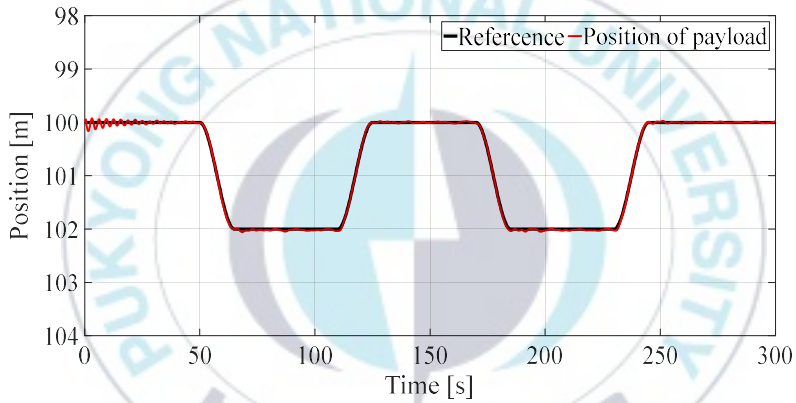


Figure 5-9. Payload position response with UUB+IOLC

Analyzing the errors obtained from these two responses, we can conclude that the ISMC and UUB-IOLC control systems damped out the residual vibration rapidly. More specifically, the ISMC control system works more effectively compared to UUB-IOLC control system.

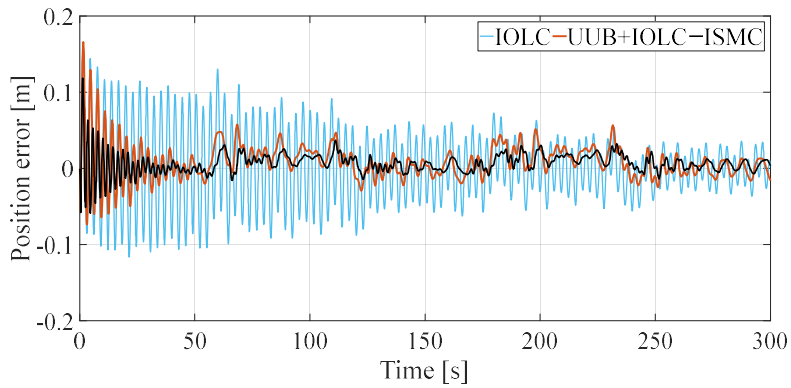


Figure 5-10. Payload position error

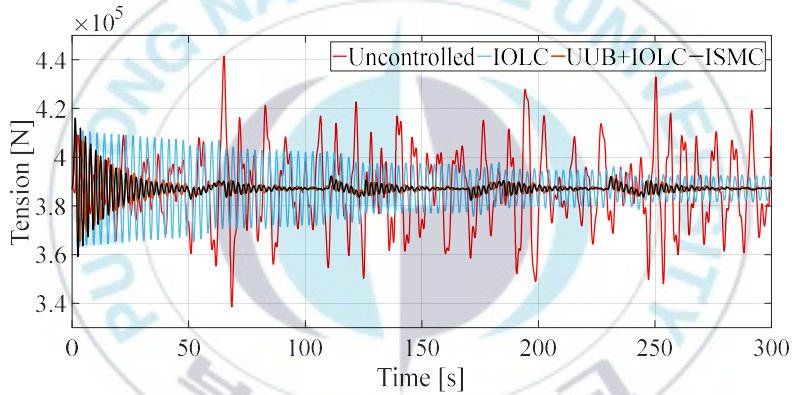


Figure 5-11. Rope tension reponse

5.2.2 Simulation with Uncertain Model

In reality, the system parameters cannot be precisely measured. Therefore, the controllers should be designed to be sufficiently robust under parametric variations. Then, it is reasonable to conduct a simulation to evaluate the robustness of the control system in an uncertain condition. In this section, the simulation with an uncertain model is conducted to evaluate

the robustness of the designed control system. The system parameters are given in Table 5-4. 2^6 sets of parameters are considered, these sets represent the endpoints [min-max] of the rectangular grid in a 6-dimension space.

The uncertain model simulation is conducted in MATLAB/Simulink. The performance index results of the simulation tests are listed in Table 5-5. In the IOLC controller case with the uncertain model, we note that the control

Table 5-4. Parameter variation range

Parameter	Nominal Value	Variation range		%
		[min	max]	
m	43,200	[30240	56160]	30
C_p	1.5	[1.05	1.95]	40
V_p	4	[2.8	5.2]	30
EA_r	4.55×10^7	[4.095	$5.005] \times 10^7$	10
C_D	1	[0.6	1.4]	40
A_p	5	[3.5	6.5]	30
Wave height	3	6		100

Table 5-5. Performance index of each controller

$J = \int_0^{\infty} e_p(t) $	Uncontrolled	IOLC	UUB+IOLC	ISMC
Maximun	276.5302	384.1713	15.5990	17.0170
Mean	268.9762	73.5736	8.7656	13.3797
Standard deviation	4.7334	94.6173	4.1439	2.0712

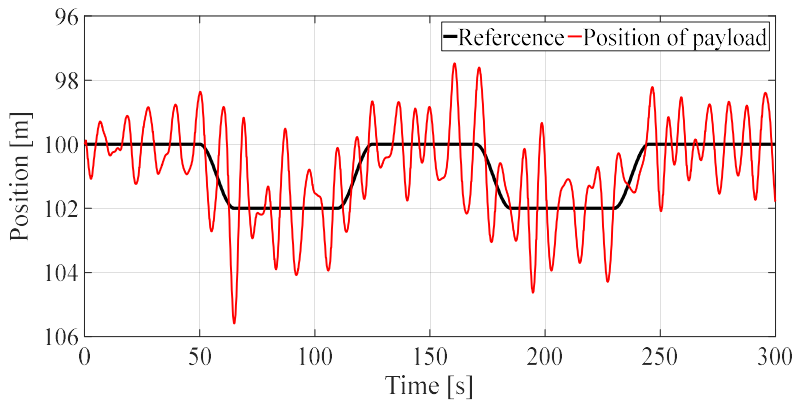


Figure 5-12. Payload position response without compensation controller for uncertain model

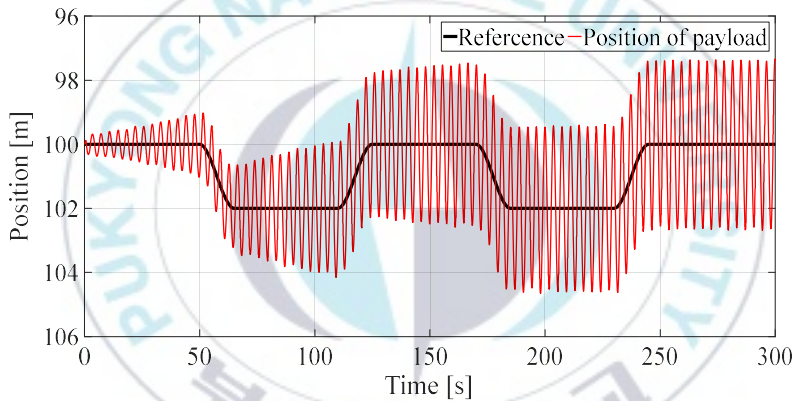


Figure 5-13. Payload position response with IOLC for uncertain model

system is not robust. Unlike the simulation results with the nominal model, the overall performance index value of the UUB+IOLC controller is smaller than that of the ISMC. Note that only the result of the ‘Maximum’ value in Table 5-5 will be introduced in the future.

Figure 5-12~Figure 5-17 present the simulation results with the uncertain model. Figure 5-12 represents the payload position response without a compensation controller. We note that the amplitude of the

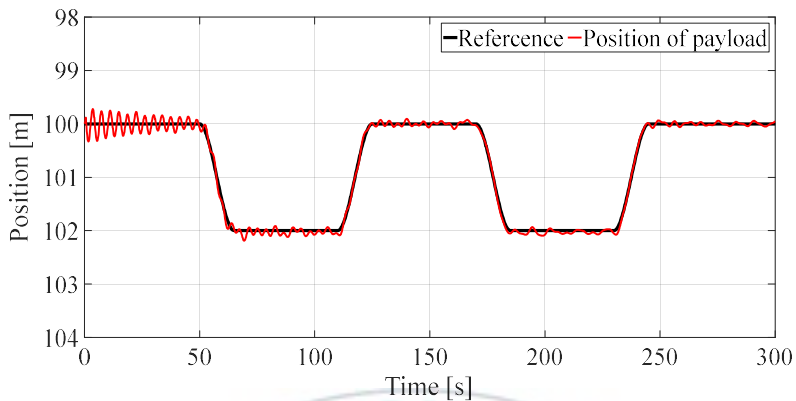


Figure 5-14. Payload position response with UUB+IOLC for uncertain model

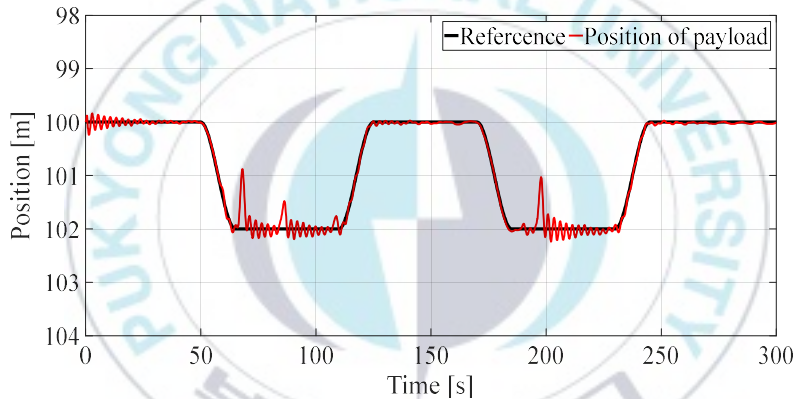


Figure 5-15. Payload position response with ISMC for uncertain model

response is larger than the nominal model case since the wave height has been increased. Figure 5-13~Figure 5-15 represent the control system's payload position response with IOLC, UUB+IOLC, and ISMC, respectively.

The control system with the IOLC was unable to drive the payload to the desired position. Moreover, the payload behavior compared to the uncontrolled case has deteriorated. However, as shown in Table 5-5, the IOLC control system can cope with wave disturbances but not as well as the

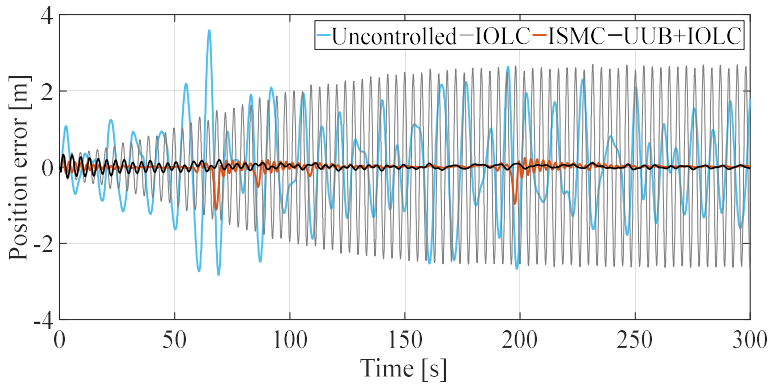


Figure 5-16. Uncertain model payload position error

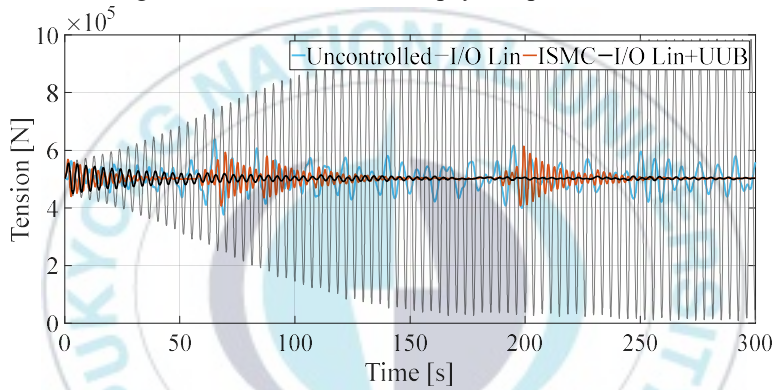


Figure 5-17. Rope tension response for uncertain model

other control systems. Hence, this control system turned out to be non-robust facing parametric variations.

In Figure 5-14~Figure 5-17, it is clear that both cases can actively cope with parametric variations. However, in the ISMC case, the controller cannot cope with the disturbance when its amplitude changes rapidly (refer to Figure 5-12 and Figure 5-15 at 67sec and 197sec). The reason of this outcome can be explained as follows. Since UUB-IOLC control system includes the disturbance decoupling term; it works more effectively than the ISMC facing strong disturbances.

6 Experiment with the Pilot Model

6.1 Experimental Setup

The hardware platform used as an offshore crane model is shown in Figure 6-1. The suspended payload is lifted and lowered by a winch system, which consists of a DC motor, an encoder, and motor driver. The encoder measures the rope length, the load cell—suspended in the air with the rope—measures the rope tension, and the Euler angles are measured with a gyro sensor. The specifications of the experimental apparatus are given in Table 6-1. The control system is implemented on the computer installed NI LabVIEW software and the PCI-6259 data acquisition board. The hardware configuration diagram for control system is illustrated in Figure 6-2.

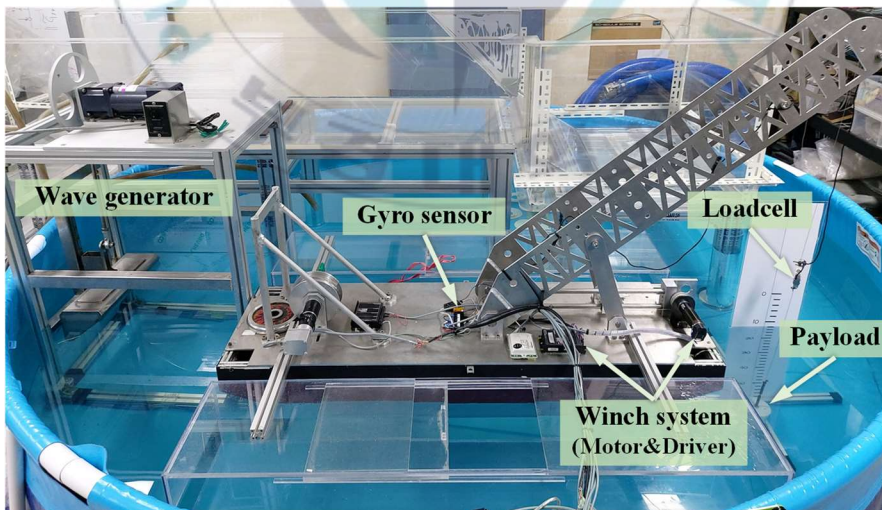


Figure 6-1. Pilot offshore crane model and wave basin for experiment

Table 6-1. Experimental apparatus specification of the offshore crane model

Item	Parameter	Value	Item	Parameter	Value
Winch System	Motor: Maxon (334067) Driver: ESCON 50/5		Load cell	CAS(CSBA-1LS)	
	Rated voltage	24[V]		Capacity	1[kgf]
	Rated power	90[W]		Rated output	1.0±0.2[mV/V]
	Rated torque	0.105[N.m]		CAS(LCT-II)	
	Rated speed	7750[rpm]	Load cell transducer amplifier	Output	0~5[V]
	Gear ratio	28:1		Accuracy	±0.02%
	Resolution	500[ppr]		Linearity	±0.02%
	Drum radius	0.025[m]			
DAQ	National Instrument (PCI-6259)		Gyro	NTRex(MW-AHRS)	
	ADC resolution	16[bits]		Euler angle's resolution	0.01[deg]
Inserted spring (1EA)	Sample rate (single chan.)	1.25[MS/s]	Response time	<1[ms]	
	Mass	0.004[kg]	Offshore crane	y_{tip}^b	0.913[m]
	Spring constant	130.8[N/m]		Nominal payload (1EA)	Mass

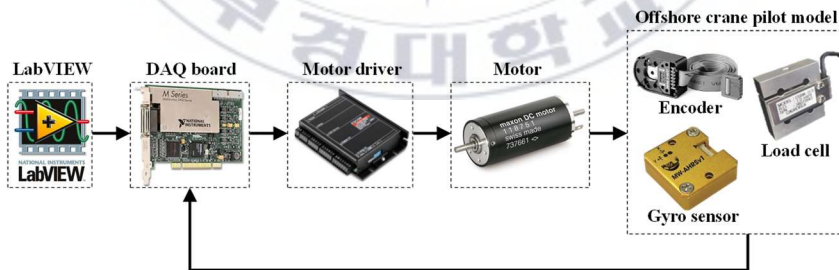


Figure 6-2. The hardware configuration diagram of the control system

The unknown parameters of the pilot model are identified through experiments and simulations.

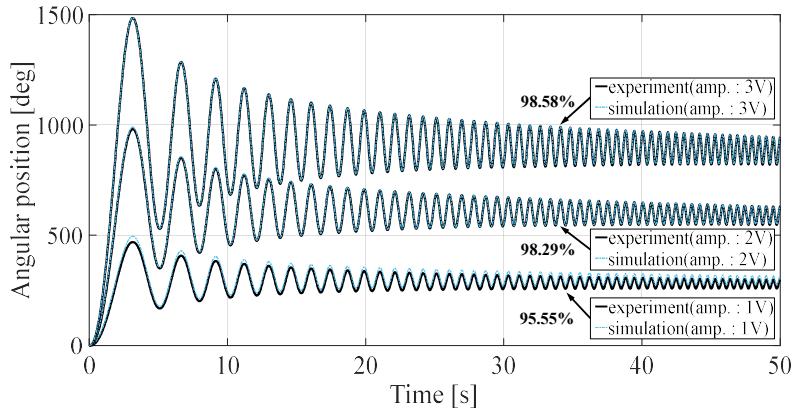


Figure 6-3. Comparison result between experiment and simulation result of actuator

Firstly, in order to identify the model of actuator consisted of motor driver and motor, input the chirp signal with 0.1[Hz] to 2[Hz] and the amplitude of 1[V], 2[V] and 3[V] into the actuator. Input signal[V] and angular position[deg] is measured and recorded. Using every data set of the input signal and the motor's angular position, we estimated the actuator's model by using the MATLAB identification toolbox. We choose the model with the best fitness rate. Figure 6-3 shows the correlation between experimental response and simulation response of the selected actuator model. The model equation of the actuator is given as

$$\ddot{\theta} + 102.8\dot{\theta} + 0.1444\theta = 26371u_w \quad (4-55)$$

The wave generator is positioned at the aft of the pilot vessel to focus on the movement along one axis; the wave encounter angle is 0deg. Hence, the pitch angle of the vessel caused by the wave may become the dominant motion. In order to configure the wave disturbance, the output of the

Table 6-2. Wave disturbance used in the experiment

Output	20%	40%	60%	80%
Wave frequency[Hz]	0.4778	0.8897	1.1494	1.5244
Wave height amplitude[m]	0.05			

generated wave is successively 20%, 40%, 60%, and 80% of the total capacity. The reciprocating displacement of the wave generator's piston is at 0.1[m]. The frequency and height of the produced wave disturbance are listed in Table 6-2.

The FFT results of the vessel's roll and pitch motion for each output are shown in Figure 6-4 and Figure 6-5. In this figure, the pitch angle amplitude appears the largest when the output is at 40%. However, when the output is at 80%, the pitch angle is so small as to be negligible; therefore, it is excluded from the experimental procedure. Furthermore, the roll motion can be neglected since its amplitude is too small.

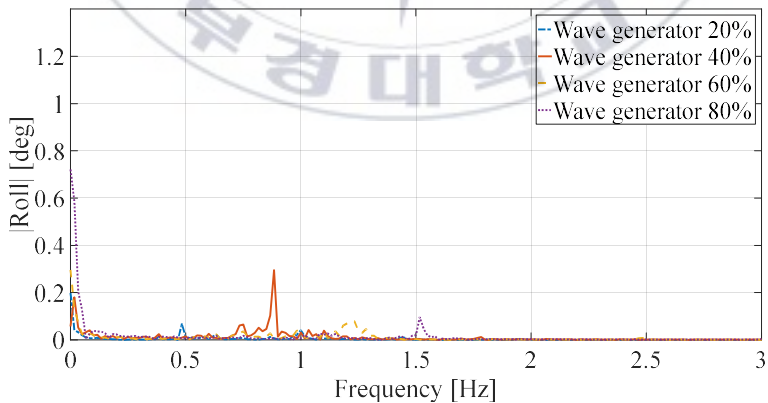


Figure 6-4. FFT results of the roll motion

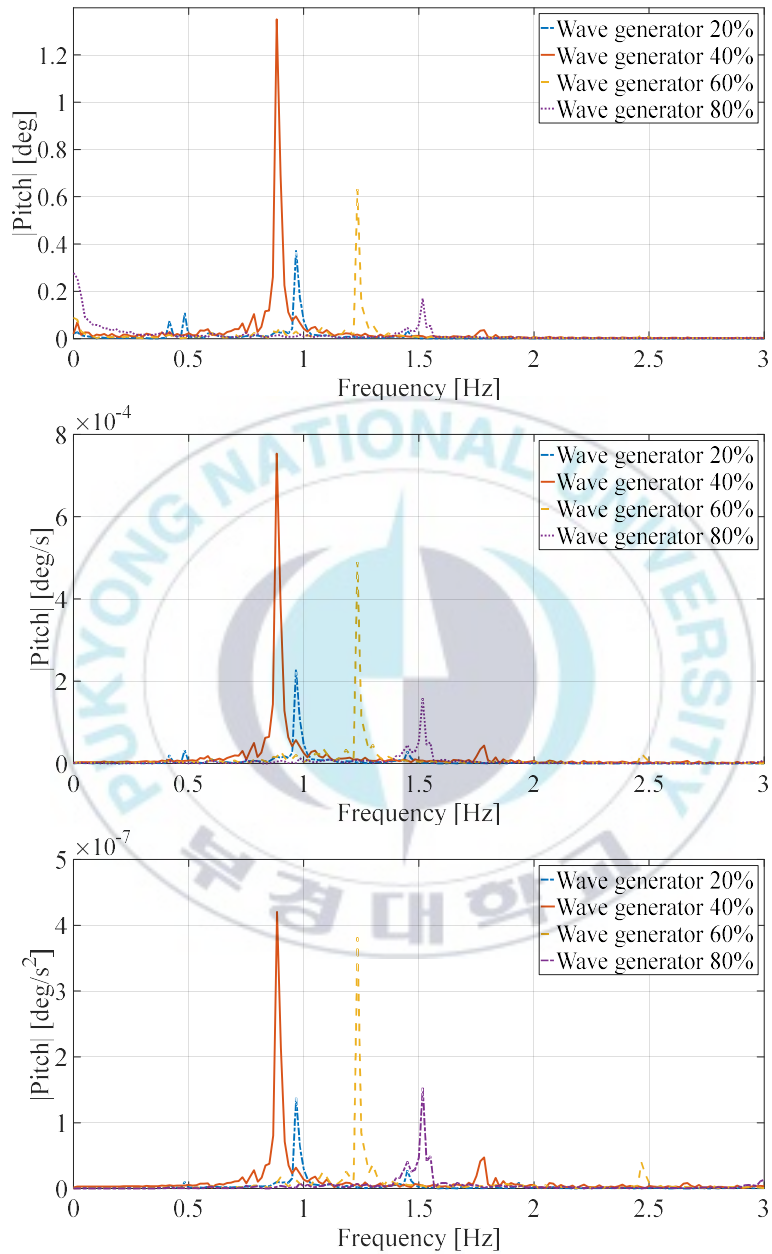


Figure 6-5. FFT results of the pitch motion (angle, angular velocity and acceleration)

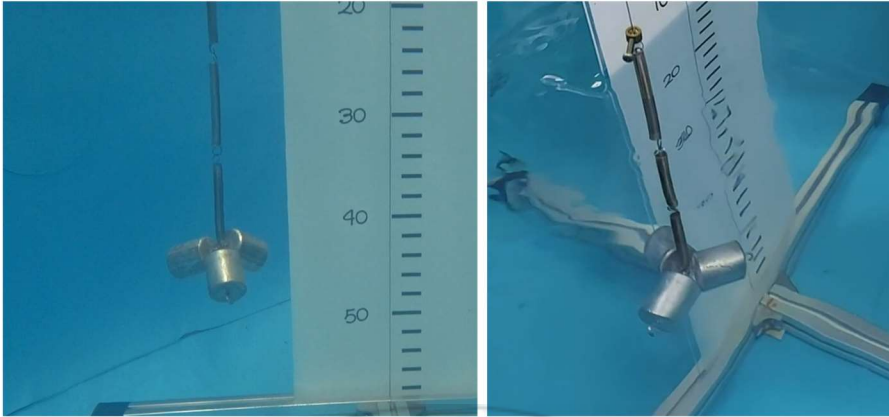


Figure 6-6. Payload used in experiments

In the experiment of the nominal model, three weights and three springs are attached to the crane system, as shown in Figure 6-6.

The total payload is 0.6kg and the equivalent spring constant is 43.6N/m. After careful analysis, the hydrodynamic coefficients are identified as the following $C_a = 0.4$, $C_D = 1$.

Following the same procedure as the simulation study, the payload's desired position p_{ref}^n is set to alternate a 0.2[m] ascending motion for 3 seconds and 0.2[m] descending motion after 20 seconds with $|\ddot{\theta}_d|_{\max} = 6$ rad/s². Note that when the wave generator's output is at 40%, the desired position is set to only be 0.1[m] due to limitations of the experimental basin's depth. Therefore, using the third-order Hermite interpolation, the resulting desired position of the payload is illustrated in Figure 6-7.

Using this experimental configuration, the controller gains for the experiment are obtained and listed in Table 6-3.

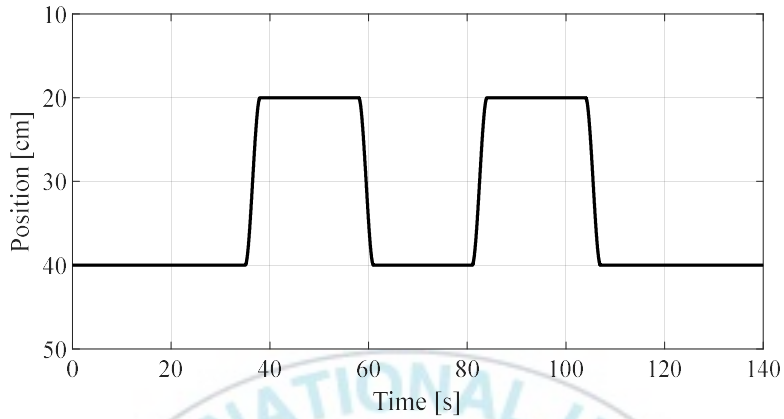


Figure 6-7. Desired position of the payload used in experiment

Table 6-3. Controller gain used in experiment

Controller	Gain
IOLC	$q_1 = 7000, q_2 = 300, R = 0.02$ $\rightarrow k_1 = 127.213, k_2 = 591.608$ $k_1 = 127.213, k_2 = 591.608$
UUB-IOLC	$\sigma = 0.0005, k_3 = 0.1, k_4 = 0.001,$ $c_1 = 6.49158, c_2 = 2.083, \varepsilon = 0.0005$
ISMC	$g_1 = 0.01, g_2 = 1, g_3 = 40,$ $g_4 = 700, g_5 = 50, \eta = 0.44 (K = 0.5)$

6.2 Experimental Results

6.2.1 Experiment with the Nominal Model

Table 6-4. Performance index of each wave conditions

Output of wave generator	$J = \int_0^{\infty} e_p(t) $		
	20%	40%	60%
Uncontrolled	160.1272	452.0344	355.5983
IOLC	102.4312	326.7183	137.3719
UUB+IOLC	55.023	190.8782	85.2664
ISMC	64.5909	250.9576	98.21

Using measured data from experiment results, the performance index $J = \int_0^{\infty} |e_p(t)|$ is calculated and the results are listed in Table 6-4. Note that only the results of the 40% of the output case will be introduced in details following the same procedure as the simulation study.

Experiment results with the nominal model are presented in Figure 6-8~Figure 6-12. Figure 6-8~Figure 6-11 show the payload position response. In these figures, during the first 15 seconds of the experiment, the controller is switched off. Thereafter, the controller is activated to drive the payload to its desired position. Figure 6-13 shows the position error of the payload, and Figure 6-12 shows the rope tension response.

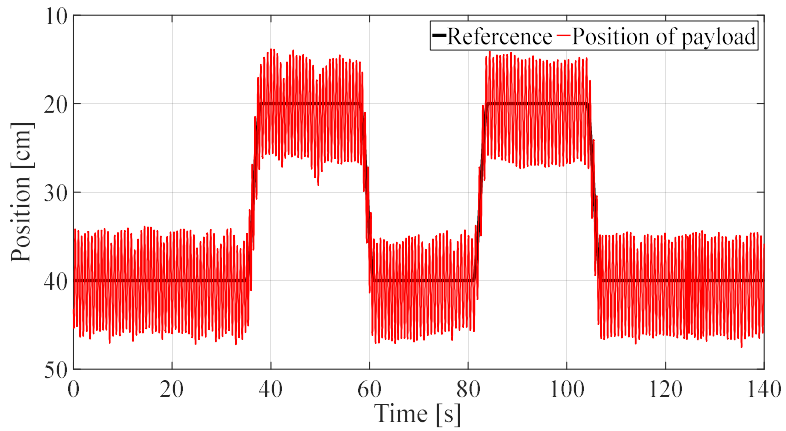


Figure 6-8. Payload position response from the experiment without compensation controller

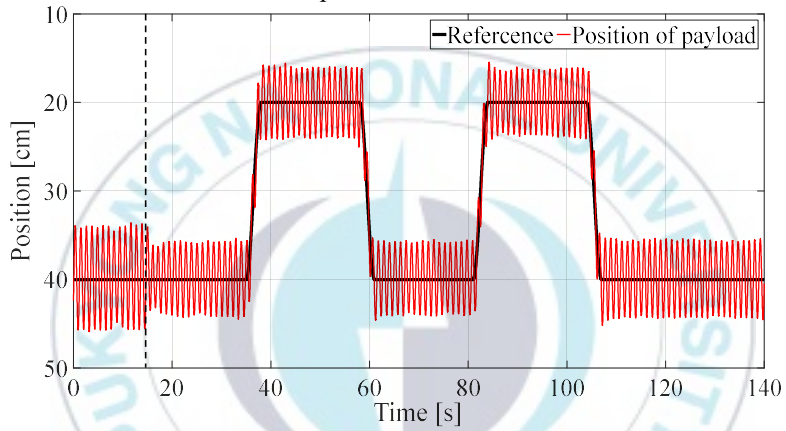


Figure 6-9. Payload position response from the experiment with IOLC

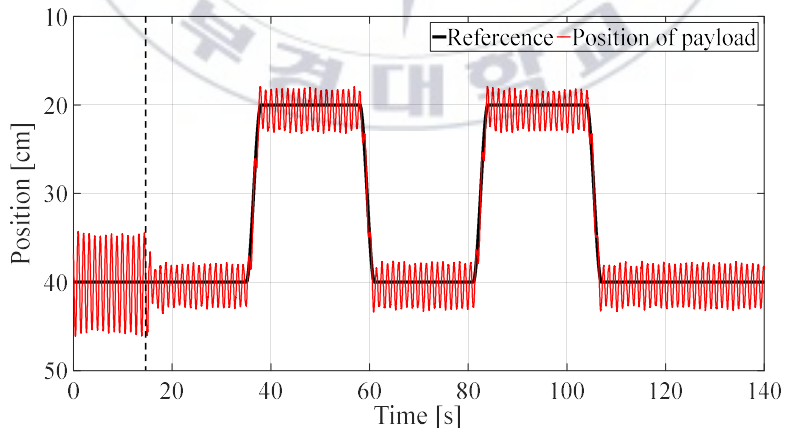


Figure 6-10. Payload position response from the experiment with UUB+IOLC

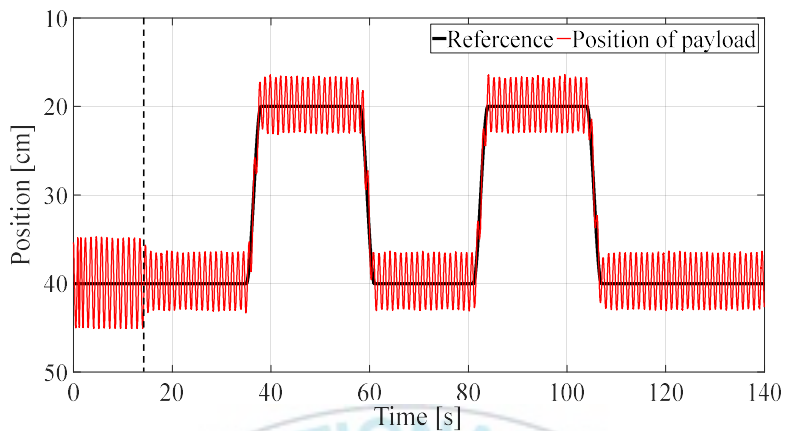


Figure 6-11. Payload position response from the experiment with ISMC

As mentioned earlier, Figure 6-8 depicts the payload position response without the compensation controller. In this figure, the payload position is of the same amplitude all until the end of the experiment. However, in the controlled cases, shown in Figure 6-9~Figure 6-12, the payload position, as well as the rope tension amplitude, are swiftly suppressed. From Figure 6-9~Figure 6-12, one can conclude the performance of the UUB+IOLC is superior to that of the other controllers.

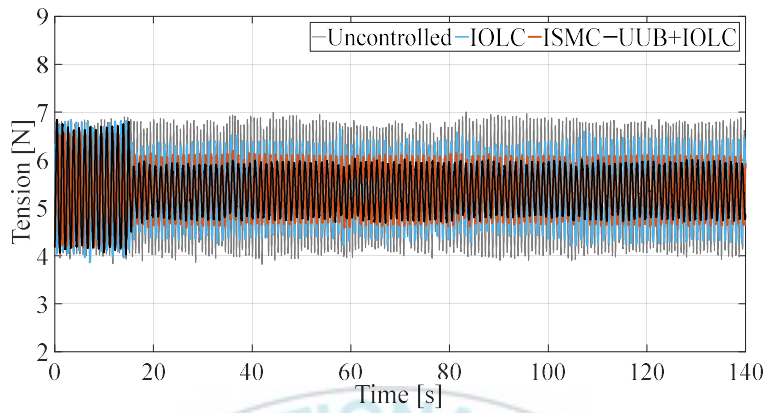


Figure 6-12. Rope tension response from the experiment

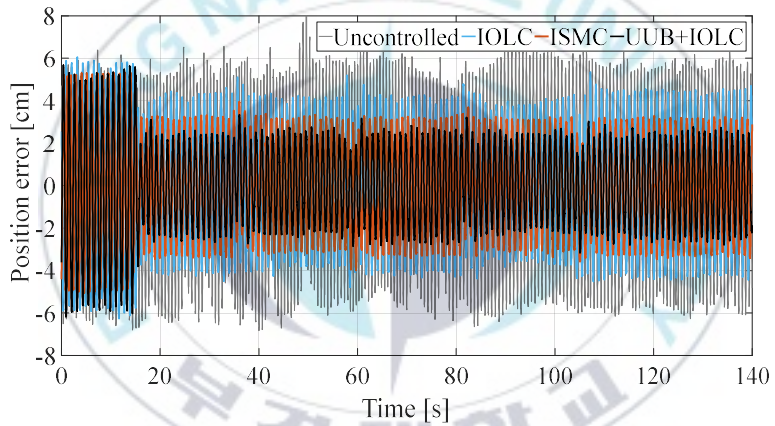


Figure 6-13. Payload position error from experiment

6.2.2 Experiment with the Uncertain Model

In this section, the robust analysis previously stated is tested through experiments. To configure the parametric variations, two different 3D printed models of the payload are introduced, as shown in Figure 6-14 and Figure 6-15, and 3D drawing is depicted in Figure 6-16 and Figure 6-17. The weight could be suspended in the center of the 3D printed model. The 3D printed models are inspired by the subsea installation, drilling, and pipe laying structures. The real systems are shown in Figure 6-18[50], [51]. Additionally, the number of weights and springs has been reduced, respectively, by two. That is, the inserted weight is 0.4kg, and the equivalent spring constant is 65.4N/m.

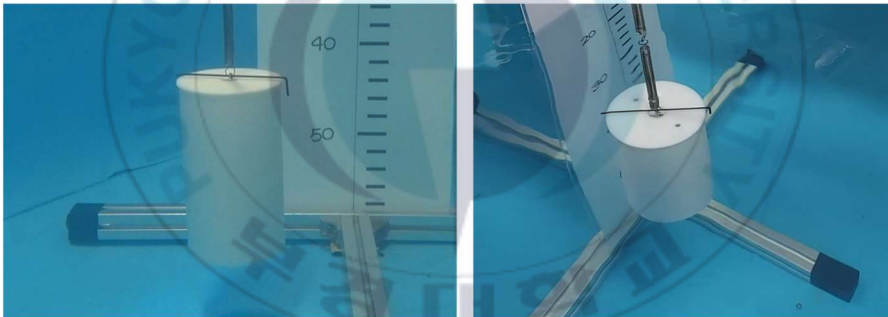


Figure 6-14. Suction pile: 3D printed model for the configuration of parametric variation

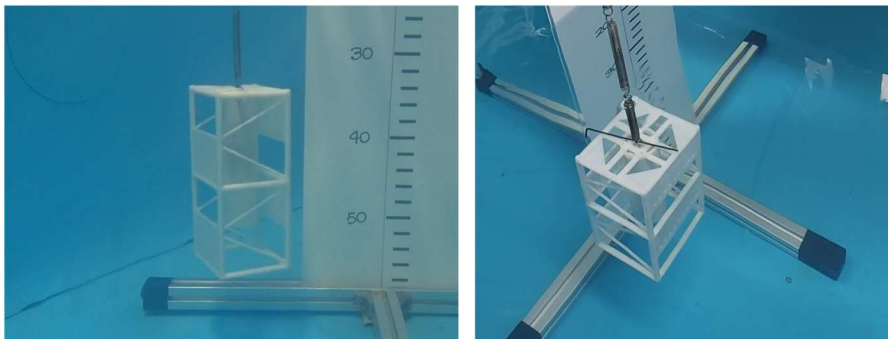
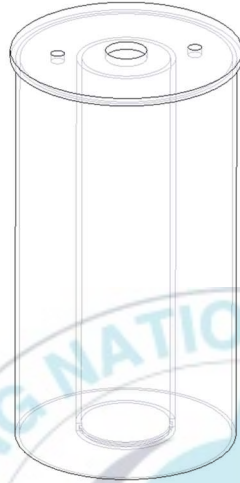
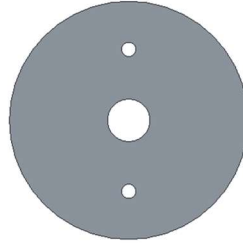


Figure 6-15. Manifold: 3D printed model for the configuration of parametric variation

Isometric view



Top view



Bottom view

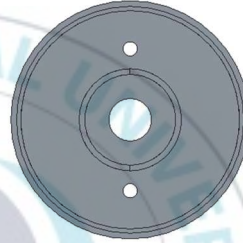
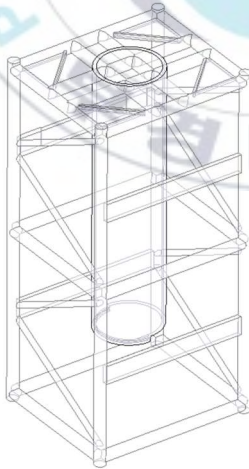
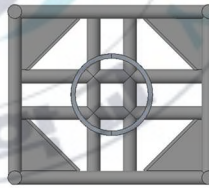


Figure 6-16. 3D drawing of suction pile

Isometric view



Top view



Bottom view

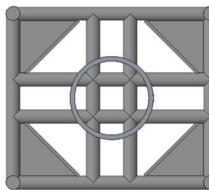


Figure 6-17. 3D drawing of manifold



Figure 6-18. Example of the actual subsea installation system (left: suction pile, right: manifold)

Using the obtained controller gains and the system configuration as in the experiments with the nominal model, The same procedure as the previous section has been adopted in the new set of experimental tests. The performance index is calculated using the measured data from the experiment, the results are shown in Table 6-5.

Table 6-5. Performace index of each wave condition and payload shape

Output of wave generator		$J = \int_0^{\infty} e_p(t) $		
		20%	40%	60%
Suction pile	Uncontrolled	83.7806	438.7291	137.7685
	IOLC	40.5978	214.4034	84.1417
	UUB+IOLC	38.0967	133.635	56.6176
	ISMIC	32.0787	169.8621	64.0237
Manifold	Uncontrolled	67.5714	382.9903	187.334
	IOLC	62.0795	237.8163	134.8257
	UUB+IOLC	44.4611	159.489	104.9172
	ISMIC	44.2838	187.1458	112.669

As shown in this table, if the wave disturbance is not strong—when the output is at 20%—the performance of the ISMC is superior to all other controllers. Otherwise, the UUB+IOLC works more effectively better than all the designed control systems. Note that only the results of the 40% case with the suction pile will be introduced since it represents the worst case.

The experiment results with the uncertain model are presented in Figure

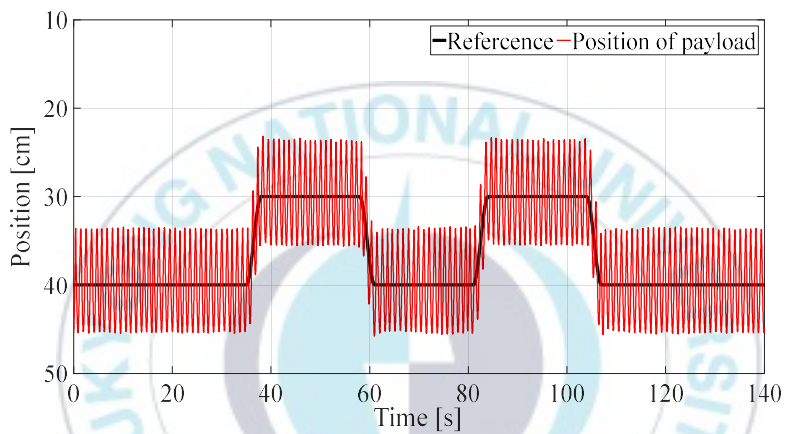


Figure 6-19. Payload position response from the uncertain model experiment without compensation controller

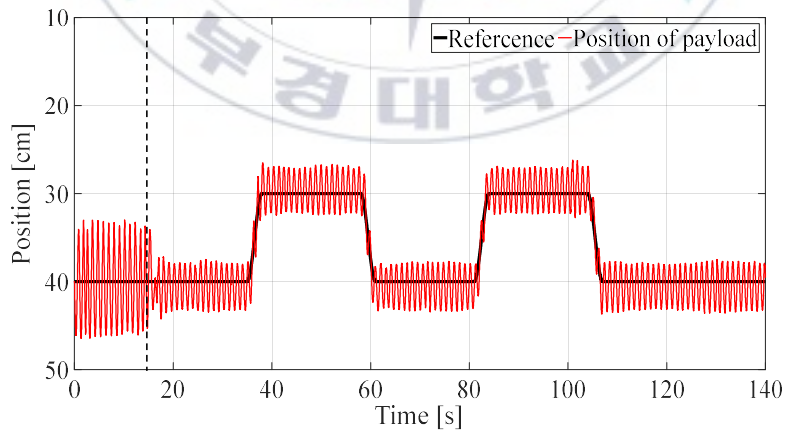


Figure 6-20. Payload position response from the uncertain model experiment with IOLC

6-19~Figure 6-24. Figure 6-19~Figure 6-22 show the payload position response. Figure 6-23 and Figure 6-24 show, respectively, the position error of the payload and the rope tension response.

The experimental results with the uncertain model emphasize the findings of the previous section. In Figure 6-24, the rope tension variation range while the controller is switched off is massive in comparison with the

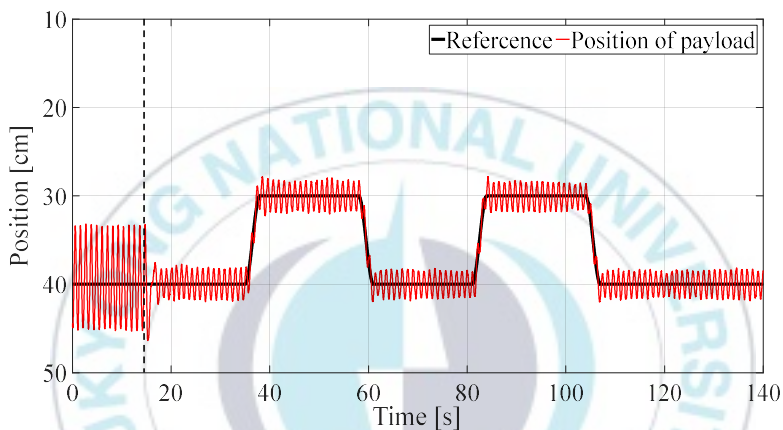


Figure 6-21. Payload position response from the uncertain model experiment with UUB+IOLC

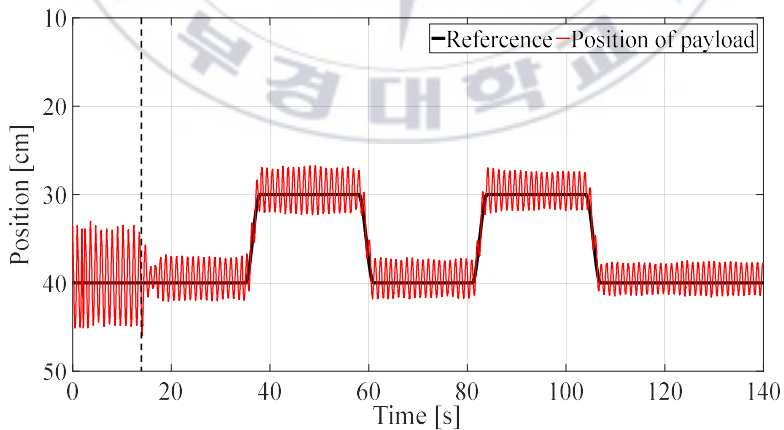


Figure 6-22. Payload position response from the uncertain model experiment with ISMC

nominal model case. Nevertheless, after the controller is switched on, the tension variation is suppressed effectively. However, as shown in Figure 6-23 and Figure 6-24, the IOLC control system could not damp down the position error and rope tension. On the other hand, the UUB+IOLC and ISMC control systems gradually decrease the amplitude of the rope tension and the payload position error.

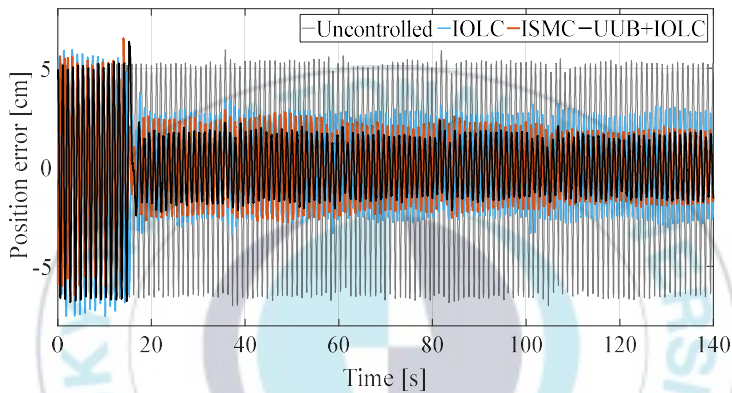


Figure 6-23. Payload position error from the uncertain model experiment

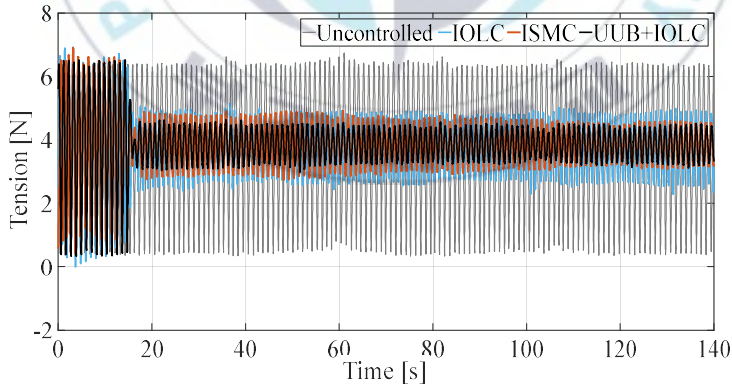


Figure 6-24. Rope tension response from the uncertain model experiment

7 Conclusion and Future Study

7.1 Conclusion

The main purpose of the study is to suggest a control system design for the offshore crane system to cope with disturbances and parametric variations.

The modeling of the offshore crane system was approached in chapter 3. Three control systems were introduced in chapter 4. The performance of the designed control system was evaluated through simulation and experimental results in chapters 5 and 6, respectively.

In chapter 3, input-output linearization controller(IOLC), uniformly ultimate boundedness controller (UUB+IOLC) and integral sliding mode controller(ISMC) are introduced. The input-output linearization controller for active heave compensation has been previously studied in [9], [10]. As mentioned before, this control technique cannot be robust if the nonlinearity is uncertain.

For this reason, the uniformly ultimate boundedness controller is proposed to improve the control performance and ensure robustness. Therefore, the proposed control system consists of two components. One is the control law of IOLC, and the other control law is derived from an energy-based Lyapunov function. The design procedure of the controller is achieved following the proper definition of the system's output and state. Closed-loop

system analysis is given, showing that the proposed control law can satisfy uniformly ultimate boundedness of the output function and the rope variations.

Additionally, an integral sliding mode controller was also designed for the offshore system in order to compare the characteristics and performance of the proposed control system.

Using the designed control systems, simulations and experiments were conducted with a nominal model and an uncertain model.

In comparison with other control systems, the simulation and experimental results both validate the effectiveness of the uniformly ultimate unboundedness controller in suppressing the rope variations and in improving the payload positioning performance.

7.2 Future Study

As for this thesis, future works are listed as follow,

Control system

- Control system design in combination with real-time prediction technique such as Kalman filter and model predictive control to overcome the delay caused by sensor and signal processing.
- Control system design with gain real-time optimization technique to improve and ensure the control performance regardless of

uncertainties(disturbance, parametric variation, etc.).

Mechanism

- Design the full(multi) dimensional compensation structure for the offshore crane to achieve accurate load positioning.



References

- [1] J. G. Balchen, N. A. Jenssen, E. Mathisen, and S. Sælid, "A Dynamic Positioning System Based on Kalman Filtering and Optimal Control," *Model. Identif. Control A Nor. Res. Bull.*, vol. 1, no. 3, pp. 135–163, May 1980.
- [2] T. I. Fossen and J. P. Strand, "Nonlinear passive weather optimal positioning control (WOPC) system for ships and rigs: Experimental results," *Automatica*, vol. 37, no. 5, pp. 701–715, 2001.
- [3] K. D. Do, Z. P. Jiang, and J. Pan, "Universal controllers for stabilization and tracking of underactuated ships," *Syst. Control Lett.*, vol. 47, no. 4, pp. 299–317, Nov. 2002.
- [4] A. J. Sørensen, "Structural issues in the design and operation of marine control systems," *Annu. Rev. Control*, vol. 29, no. 1, pp. 125–149, Jan. 2005.
- [5] Heerema, "Aegir Experiences Dropfall Incident," *Heerema Marine Contractors*, 2020. [Online]. Available: <https://hmc.heerema.com/news-media/news/aegir-experiences-dropfall-incident/>.
- [6] N. Ugal, "Larsen & Toubro confirms heavy-lift vessel incident," *upstream*, 2020. [Online]. Available: <https://www.upstreamonline.com/safety/larsen-toubro-confirms-heavy-lift-vessel-incident/2-1-774155>.
- [7] F. R. Driscoll, M. Nahon, and R. G. Lueck, "A Comparison of Ship-

Mounted and Cage-Mounted Passive Heave Compensation Systems,” *J. Offshore Mech. Arct. Eng.*, vol. 122, no. 3, pp. 214–221, Aug. 2000.

- [8] F. R. Driscoll, B. Buckham, and M. Nahon, “Numerical optimization of a cage-mounted passive heave compensation system,” in *OCEANS 2000 MTS/IEEE Conference and Exhibition. Conference Proceedings (Cat. No.00CH37158)*, 2007, vol. 2, no. 3, pp. 1121–1127.
- [9] S. KÜchler, T. Mahl, J. Neupert, K. Schneider, and O. Sawodny, “Active Control for an Offshore Crane Using Prediction of the Vessel’s Motion,” *IEEE/ASME Trans. Mechatronics*, vol. 16, no. 2, pp. 297–309, Apr. 2011.
- [10] J. Neupert, T. Mahl, B. Haessig, O. Sawodny, and K. Schneider, “A heave compensation approach for offshore cranes,” in *2008 American Control Conference*, 2008, pp. 538–543.
- [11] S. Messineo, F. Celani, and O. Egeland, “Crane feedback control in offshore moonpool operations,” *Control Eng. Pract.*, vol. 16, no. 3, pp. 356–364, Mar. 2008.
- [12] S. Messineo and A. Serrani, “Offshore crane control based on adaptive external models,” *Automatica*, vol. 45, no. 11, pp. 2546–2556, Nov. 2009.
- [13] S. I. Sagatun, T. A. Johansen, T. I. Fossen, and F. G. Nielsen, “Wave synchronizing crane control during water entry in offshore moonpool operations,” in *Proceedings of the International*

- Conference on Control Applications*, 2002, vol. 1, no. 3, pp. 174–179.
- [14] T. A. Johansen, T. I. Fossen, S. I. Sagatun, and F. G. Nielsen, “Wave synchronizing crane control during water entry in offshore moonpool operations-experimental results,” *IEEE J. Ocean. Eng.*, vol. 28, no. 4, pp. 720–728, Oct. 2003.
- [15] K. D. Do and J. Pan, “Nonlinear control of an active heave compensation system,” *Ocean Eng.*, vol. 35, no. 5–6, pp. 558–571, Apr. 2008.
- [16] M. A. Ahmad, M. S. Ramli, R. M. T. R. Ismail, R. E. Samin, and M. A. Zawawi, “Implementation of input shaping in hybrid control schemes of a lab-scaled rotary crane system,” in *2010 IEEE International Conference on Industrial Technology*, 2010, pp. 530–534.
- [17] E. Maleki and W. Singhose, “Dynamics and control of a small-scale boom crane,” *J. Comput. Nonlinear Dyn.*, vol. 6, no. 3, pp. 1–8, 2011.
- [18] Z. N. Masoud and M. F. Daqaq, “A Graphical Approach to Input-Shaping Control Design for Container Cranes With Hoist,” *IEEE Trans. Control Syst. Technol.*, vol. 14, no. 6, pp. 1070–1077, Nov. 2006.
- [19] S. D. Jones and A. G. Ulsoy, “An Approach to Control Input Shaping With Application to Coordinate Measuring Machines,” *J. Dyn. Syst. Meas. Control*, vol. 121, no. 2, pp. 242–247, Jun. 1999.

- [20] N. Sun, Y. Fang, X. Sun, and Z. Xin, "An energy exchanging and dropping-based model-free output feedback crane control method," *Mechatronics*, vol. 23, no. 6, pp. 549–558, Sep. 2013.
- [21] M. S. Park and D. Chwa, "Swing-up and stabilization control of inverted-pendulum systems via coupled sliding-mode control method," *IEEE Trans. Ind. Electron.*, vol. 56, no. 9, pp. 3541–3555, 2009.
- [22] Dongkyoung Chwa, "Nonlinear Tracking Control of 3-D Overhead Cranes Against the Initial Swing Angle and the Variation of Payload Weight," *IEEE Trans. Control Syst. Technol.*, vol. 17, no. 4, pp. 876–883, Jul. 2009.
- [23] A. Isidori, *Nonlinear Control Systems*, 3rd Ed. London: Springer, 1995.
- [24] Hamid Reza Karimi, "Robust Feedback Linearization Control for a non Linearizable MIMO Nonlinear System in the Presence of Model Uncertainties," in *2006 IEEE International Conference on Service Operations and Logistics, and Informatics*, 2006, pp. 965–970.
- [25] H. Guillard and H. Bourlès, "Robust feedback linearization," in *Proceedings of the 14th International Symposium of Mathematical Theory of Networks and Systems*, 2000, no. June.
- [26] A. L. D. Franco, H. Bourlès, and E. R. De Pieri, "Robust Feedback Linearization without Full State Information," *IFAC Proc. Vol.*, vol. 40, no. 20, pp. 70–75, 2007.

- [27] H. K. Khalil, *Nonlinear Systems*, 3rd Ed. East Lansing: Pearson, 2002.
- [28] J. Kennedy and R. Eberhart, "Particle swarm optimization," in *Proceedings of ICNN'95 - International Conference on Neural Networks*, 1995, vol. 4, no. 1, pp. 1942–1948.
- [29] R. C. Eberhart, P. K. Simpson, and R. W. Dobbins, *Computational Intelligence Pc Tools*. Academic Press Professional, 1996.
- [30] P. Goldstein, "It's birds, it's a plane, it's...? Photographer captures stunning Starling murmuration," *KOMONEWS*, 2018.
- [31] X. Hu, "PSO Tutorial," 2006. [Online]. Available: <http://www.swarmintelligence.org/tutorials.php>.
- [32] T. I. Fossen, *Handbook of Marine Craft Hydrodynamics and Motion Control*. Chichester, UK: John Wiley & Sons, Ltd, 2011.
- [33] D. T. Greenwood, *Principles of Dynamics*. Prentice Hall, 1988.
- [34] S. KÜchler and O. Sawodny, "Nonlinear control of an active heave compensation system with time-delay," in *2010 IEEE International Conference on Control Applications*, 2010, pp. 1313–1318.
- [35] Y. Fang, P. Wang, N. Sun, and Y. Zhang, "Dynamics analysis and nonlinear control of an offshore boom crane," *IEEE Trans. Ind. Electron.*, vol. 61, no. 1, pp. 414–427, 2014.
- [36] Q. H. Ngo, N. P. Nguyen, C. N. Nguyen, T. H. Tran, and V. H. Bui, "Payload pendulation and position control systems for an offshore container crane with adaptive-gain sliding mode control," *Asian J. Control*, vol. 22, no. 5, pp. 2119–2128, Sep. 2020.

- [37] K. S. Hong and Q. H. Ngo, "Dynamics of the container crane on a mobile harbor," *Ocean Eng.*, vol. 53, pp. 16–24, 2012.
- [38] Y. Qian and Y. Fang, "Dynamics analysis of an offshore ship-mounted crane subject to sea wave disturbances," *Proc. World Congr. Intell. Control Autom.*, vol. 2016-Sept, pp. 1251–1256, 2016.
- [39] E. Yh, L. Ws, E. Low, and S. Ggl, "Identification of the Hydrodynamics Coefficients of an Underwater Vehicle using Free Decay Pendulum Motion," in *Proceedings of the International MultiConference of Engineers and Computer Scientists*, 2008, vol. 2.
- [40] W. R. Abdul-Adheem and I. K. Ibraheem, "Decoupled control scheme for output tracking of a general industrial nonlinear MIMO system using improved active disturbance rejection scheme," *Alexandria Eng. J.*, vol. 58, no. 4, pp. 1145–1156, Dec. 2019.
- [41] F. Wang, J.L. Ding, and G.-H. Liu, "A Fast Decoupling Method for Multi-input Multi-output Nonlinear Continuous-Time System," in *Lecture Notes in Computer Science (including subseries Lecture Notes in Artificial Intelligence and Lecture Notes in Bioinformatics)*, vol. 8588 LNCS, 2014, pp. 259–268.
- [42] B. Skaare and O. Egeland, "Parallel Force/Position Crane Control in Marine Operations," *IEEE J. Ocean. Eng.*, vol. 31, no. 3, pp. 599–613, Jul. 2006.
- [43] D. H. Lee, T. W. Kim, H. C. Park, and Y. B. Kim, "A study on the

- modeling and dynamic analysis of the offshore crane and payload,” *J. Korean Soc. Fish. Technol.*, vol. 56, no. 1, pp. 61–70, Feb. 2020.
- [44] S. M. Moon, J. Huh, D. Hong, S. Lee, and C. S. Han, “Vertical motion control of building façade maintenance robot with built-in guide rail,” *Robot. Comput. Integr. Manuf.*, vol. 31, no. 1, pp. 11–20, 2015.
- [45] G. Lai, G. Tao, and Y. Zhang, “Adaptive Control of Noncanonical Nonlinear Systems with Unknown Input Dead-Zone Characteristics,” in *2018 IEEE Conference on Decision and Control (CDC)*, 2018, vol. 2018-Decem, no. Cdc, pp. 5524–5529.
- [46] H. D. Tho, R. Tasaki, K. Terashima, M. Tsume, and K. Suzuki, “Robust Sliding Mode Control of a Rotary Hook,” *IFAC-PapersOnLine*, vol. 50, no. 1, pp. 6060–6066, Jul. 2017.
- [47] H. D. Tho and K. Terashima, “Robust Control Designs of Payload’s Skew Rotation in a Boom Crane System,” *IEEE Trans. Control Syst. Technol.*, vol. 27, no. 4, pp. 1608–1621, Jul. 2019.
- [48] H. D. Tho, R. Tasaki, A. Kaneshige, T. Miyoshi, and K. Terashima, “Robust Sliding Mode Control with Integral Sliding surface of an underactuated rotary hook system,” in *2017 IEEE International Conference on Advanced Intelligent Mechatronics (AIM)*, 2017, vol. 50, no. 1, pp. 998–1003.
- [49] J. J. E. Slotine and W. Li, *Applied Nonlinear Control*. New Jersey: Pearson, 1991.
- [50] Intermoor, “Which Foundation for your Pipeline Termination?”

[Online]. Available: <https://intermoor.com/press-releases/which-foundation-is-optimal-for-your-pipeline-termination/>.

- [51] STP-Offshore, “Suction piles for Subsea structures foundations.”
[Online]. Available: <https://www.sptoffshore.com/subsea-foundations/>.

